

# Emission-Line Galaxies from the Hubble Space Telescope Probing Evolution and Reionization Spectroscopically (PEARS) Grism Survey. II: The Complete Sample

Nor Pirzkal<sup>1</sup>, Barry Rothberg<sup>1,2,3</sup>

Chun Ly<sup>1,4</sup>, Sangeeta Malhotra<sup>5</sup>, James E. Rhoads<sup>5</sup>, Norman A. Grogan<sup>1</sup>, Tomas Dahlen<sup>1</sup>, Kai G. Noeske<sup>1</sup>, Gerhardt R. Meurer<sup>6</sup>, Jeremy R. Walsh<sup>7</sup>, Nimish P. Hathi<sup>8</sup>, Seth H. Cohen<sup>5</sup>, Andrea Bellini<sup>1</sup>, Benne W. Holwerda<sup>9</sup>, Amber N. Straughn<sup>10</sup>, Matthew Mechtley<sup>5</sup>, Rogier A. Windhorst<sup>5</sup>

## ABSTRACT

We present a full analysis of the Probing Evolution And Reionization Spectroscopically (PEARS) slitless grism spectroscopic data obtained with the Advanced Camera for Surveys onboard *HST*. PEARS covers fields within both the Great Observatories Origins Deep Survey (GOODS) North and South fields, making it ideal as a random survey of galaxies, as well as the availability of a wide variety of ancillary observations complemented by the spectroscopic results. Using the PEARS data we are able to identify star-forming galaxies within the redshift volume  $0 < z < 1.5$ . Star-forming regions in the PEARS survey are pinpointed independently of the host galaxy. This method allows us to detect the presence of multiple emission line regions (ELRs) within a single galaxy. We identified a

---

<sup>1</sup>Space Telescope Science Institute, 3700 San Martin Drive, Baltimore, MD, 21210, USA

<sup>2</sup>George Mason University, Department of Physics & Astronomy, MS 3F3, 4400 University Drive, Fairfax, VA 22030, USA

<sup>3</sup>Leibniz-Institut für Astrophysik Potsdam (AIP), An der Sternwarte 16, 14482, Potsdam, Germany

<sup>4</sup>Giacconi Fellow

<sup>5</sup>School of Earth And Space Exploration, Arizona State University, Tempe, AZ, 85287-1404, USA

<sup>6</sup>International Centre for Radio Astronomy Research, The University of Western Australia, 35 Stirling Highway, Crawley, WA 6009, Australia

<sup>7</sup>European Southern Observatory, Karl-Schwarzschild-Strasse 2, D-85748 Garching, Germany

<sup>8</sup>Carnegie Observatories, 813 Santa Barbara Street, Pasadena, CA 91101, USA

<sup>9</sup>ESA Fellow, ESA-ESTEC, Keplerlaan 1, 2200 AG, Noordwijk, the Netherlands

<sup>10</sup>Astrophysics Science Division, Goddard Space Flight Center, Code 665, Greenbelt, MD 20771, USA

total of 1162  $\text{H}\alpha$ , [OIII] and/or [OII] emission-lines in the PEARS sample of 906 galaxies to a limiting flux of  $\sim 10^{-18}$  erg/s/cm<sup>2</sup>. The ELRs have also been compared to the properties of the host galaxy, including morphology, luminosity, and mass. From this analysis, we find three key results: 1) The computed line luminosities show evidence of a flattening in the luminosity function with increasing redshift; 2) The star-forming systems show evidence of complex morphologies, with star formation occurring predominantly within one effective (half-light) radius. However, the morphologies show no correlation with host stellar mass; and 3) The number density of star-forming galaxies with  $M_* \geq 10^9 M_\odot$  decreases by an order of magnitude at  $z \leq 0.5$  relative to the number at  $0.5 < z < 0.9$  supporting the argument of galaxy downsizing.

*Subject headings:* line: identification, catalogs,galaxies: evolution,galaxies: luminosity function, mass function

## 1. Introduction

Emission line galaxies (ELGs) are systems selected by the presence of strong line emissions (e.g., Ly- $\alpha$  [OII], [OIII],  $\text{H}\beta$ , and  $\text{H}\alpha$ ), usually detected using narrow band or grism surveys. The strong emission lines in these galaxies trace recent star formation activity, in contrast to the star formation history and properties of the global stellar populations that can be discerned using broad band observations. A significant amount of the light originating from ELGs is contained in regions producing strong emission lines, which in turns makes these objects easily identifiable. The emission lines of ELGs also provide a convenient way to determine the redshifts of these objects. Since ELGs are selected on the basis of strong emission lines, rather than continuum emission, selecting ELGs allows one to potentially probe down to a lower luminosity — and thus lower mass — galaxies compared to broad band surveys, which tend to be limited by the luminosity of the galaxies themselves, rather than the strength of their emission lines. Assuming that ELGs are spatially distributed in a fashion similar to other galaxies, they provide a powerful tool for tracing the star formation history of the Universe (e.g., Salzer et al. 1988; Popescu et al. 1997).

The epoch  $0 < z < 1.5$  discussed in this paper is important, because star formation activity in galaxies has been observed to increase significantly as redshift increases (e.g. Madau et al. 1998; Hopkins 2004). While at higher redshifts ( $z > 2$ ), there is still some controversy as to whether the star-formation rate density (SFRD) relation flattens or decreases, the initial increase in star-formation implies that, at low  $z$ , some mechanism(s) must have occurred,

which quenched star formation. If this was not the case, massive ellipticals today would still be observed to be strongly forming many stars. There is also evidence that suggest that the interstellar medium, star formation rates and gas fractions differ between local and distant galaxies. Studying galaxy evolution at these redshifts therefore does not only require the ability to measure the star formation history of these objects, but also depends on our ability to properly sample galaxies over a wide range of masses to alleviate as many biases as possible. ELGs are ideal for such work. As noted above, these objects are easily detected in surveys and they are efficient for probing to lower stellar masses in terms of telescope time required. The wavelength range of the ACS grism used for PEARS makes it possible to identify the strong rest-frame emission lines that are well known to be a sign of vigorous star formation (e.g.  $H\alpha$ , [OIII] and [OII]) out to  $z \simeq 1.5$ . In this paper, examining  $H\alpha$ , [OIII] and [OII] emitters separately allows us to look at properties of star-forming galaxies in increasing redshift ranges. When plotted separately, these three emission lines represent proxies for the redshift bins of  $0 < z < 0.5$ ,  $0.1 < z < 0.9$ , and  $0.5 < z < 1.5$ , respectively.

Identifying ELGs has traditionally been done using narrow-band photometric filters. This technique has also been successfully applied to very high redshifts to detect Ly- $\alpha$  emitters (Rhoads et al. 2001). However, while narrow-band surveys can efficiently cover large fields-of-view to relatively faint magnitudes, they are typically limited to very small and discrete redshift ranges. This can be partially alleviated using multiple narrow band filters (e.g. See Subaru Deep Field, Ly et al. 2007), but continuous redshift coverage remains intrinsically limited in narrow-band surveys. The Probing Evolution And Reionization Spectroscopically (PEARS) slitless grism spectroscopic survey provides an unprecedented opportunity to study ELGs in a way that cannot be achieved from any ground-based observations. PEARS allows us to bypass the difficulties inherent in narrow-band filter surveys (as noted above) and the limitations imposed by varying sky-brightness and atmospheric emission lines, which can limit ground-based grism surveys, and identify ELGs based *solely* on the direct detection of emission lines in dispersed slitless spectra. As previously shown (Pirzkal et al. 2006; Straughn et al. 2008, 2009), this approach allows us to detect emission lines in very faint host galaxies, particularly sub- $m^*$  galaxies, over a very large and continuous redshift range. Since our survey is mainly limited by the line fluxes themselves, faint emission lines can be identified in galaxies that are only weakly detected (i.e. high EW emission lines) while brighter host galaxies tend to increase the local background flux, diluting fainter emission lines in the brightest hosts. The line flux limit of this survey is discussed in more details in Section 3.7. Particular to the PEARS survey, the use of multiple position angles on the sky allows us to identify emission lines using independent observations, as well as to pinpoint the exact physical location of the ELRs within each ELG. Crucially, and in addition to this,

the PEARS survey was designed to overlap with both the GOODS-N and GOODS-S fields, so that there exists a substantial amount of ancillary data available, including very deep, high-resolution broad-band imaging ranging from the UV to the infrared bands.

As we noted above, the redshift range ( $0 < z < 1.5$ ) probed by PEARS is a critical transition epoch, both in terms of star-formation histories and morphological evolution. On one hand, the PEARS grism slitless observations make it possible to efficiently identify emission lines, identify the corresponding ELRs and host ELGs. On the other hand, the GOODS ancillary data allow us to examine the morphology and physical characteristics of the ELGs. This powerful combination of data gives us an opportunity to examine the evolution of ELGs over a long period of cosmic time and over a much wider mass range than has been previously probed.

This paper is organized as follow: Section 2 briefly summarizes the PEARS observations (HST Proposal 10530, P.I. Malhotra). Section 3 describes the data reduction and analysis of the sample, including detection, extraction and identification of emission lines, as well as completeness tests. Section 4.1 presents the PEARS [OII], [OIII] and  $H\alpha$  line luminosity functions and their redshift evolution. Finally, Section 4.2 compares the properties of the PEARS host galaxies, such as morphology and luminosity, with the star formation properties discerned from the PEARS emission lines. All calculations in this paper assume  $H_0 = 70 \text{ km s}^{-1} \text{ Mpc}^{-1}$  and  $\Omega_M = 0.3$ ,  $\Omega_\Lambda = 0.7$  (Komatsu et al. 2011; Hinshaw et al. 2012). All magnitudes are given in the AB system.

## 2. Observations

The PEARS observations were obtained as part of a large *Hubble Space Telescope* (HST) proposal (200 orbits, Proposal 10530; P.I.: Malhotra). The program used the Advanced Camera for Surveys (ACS) Wide Field Camera (WFC) in conjunction with its G800L grism filter. The G800L has a resolution of  $R \simeq 69\text{-}131$ , and provides wavelength coverage of  $0.55\text{-}1.05 \mu\text{m}$  across the entire ACS/WFC field-of-view. A total of nine fields ( $\approx 11.65 \text{ arcmin}^2$  for each field) were observed for  $\approx 40,000 \text{ s}$  (20 orbits) each, split evenly between observations taken at different position angles (PA) on the sky (typically 3 per pointing). Multiple PA's are important for identifying and masking contamination from other sources in the field, and for removing spurious pixels (e.g. cosmic rays, bad pixels, etc). Four PEARS fields are within the GOODS-N field (Giavalisco et al. 2004). Five PEARS fields are within the GOODS-S field, with one PEARS field re-observing the GRAPES/HUDF field (Pirzkal et al. 2004). The combined areas of the PEARS-N and PEARS-S are  $50.24$  and  $68.84 \text{ arcmin}^2$ ,

respectively. The PEARS fields and their location within the GOODS fields are shown in Figure 1. Table 1 lists the PEARS fields positions and total exposure times.

### 3. Data Reduction and Analysis

#### 3.1. Detection of Emission Lines

PEARS emission lines were initially detected directly from combined high signal-to-noise ratio ACS grism slitless spectroscopic images. The method does not rely on, and is independent of, any imaging data or object catalog. The basic method used to identify emission lines in the PEARS data was described in Straughn et al. (2008, 2009). However, at that time, only the PEARS-S data were used. We now present the full PEARS dataset (comprising of PEARS-N and PEARS-S), which covers an area on the sky that is approximately twice as large. We have also employed a new, slightly refined version of our line identification pipeline, and are able to reach down to a slightly lower flux level than before. The detection algorithm, dubbed “PEARS-2D,” is very briefly summarized below and was applied to each of the individual 9 PEARS fields listed in Table 1:

- 1) All grism exposures obtained at the same PA on the sky are combined using the PYRAF task MULTIDRIZZLE (Koekemoer 2002). This produces a high signal-to-noise ratio image that is free of cosmic-ray and detector artifacts. This image is then smoothed using a  $13 \times 3$  median to produce a smooth high signal-to-noise ratio grism image of the field.
- 2) The smoothed image is subtracted from the combined Multidrizzle image of the field. This step essentially removes the underlying continuum emission from the dispersed spectra. The resulting continuum subtracted image is what we use to detect emission lines.
- 3) SExtractor (Bertin & Arnouts 1996) is used to identify point sources, e.g. emission lines, noise spikes, and detector artifacts in the continuum subtracted image. This step generates a list of emission line candidates for each PA.
- 4) Steps 1 though 3 are repeated separately for each available PA resulting in 3 or 4 (i.e. the number of available PAs) emission line candidates lists. A minimum of 2 PAs is required for the PEARS-2D method but additional PAs result in fewer false positives.
- 5) Using a detailed knowledge of the instrument distortions and of the dispersion relation for the G800L ACS/WFC grism, and combining the data obtained using multiple PA’s, we determine the location on the sky where each individual emission line originates (essentially where the different spectral traces cross when projected onto the sky), as well as determine the observed wavelength of each emission line. We derive a unique wavelength for each line in each of the available PA (See Figure 2 of Straughn et al. 2008).

The PEARS-2D method was applied separately to each PEARS field listed in Table 1, and a separate list of ELR candidates was therefore generated for each of the nine PEARS fields, ignoring for now the fact that some of these fields overlap slightly. The number of ELR candidates that was generated was controlled mainly by the detection threshold used to detect emission lines with SExtractor, and by how much tolerance we allowed in the inferred ELR positions and therefore the observed wavelengths of the emission lines. We adopted a detection of  $1.1\sigma$  per PA, which for a line detected independently using 3 different PA’s corresponds approximately to a  $2\sigma$  detection. We also allowed for a 3 pixel tolerance in the physical location of an ELR (accounting for an imperfect knowledge of the trace for the ACS grism), and a  $100\text{\AA}$  tolerance in the wavelength that we derive for an emission line (again accounting for an imperfect knowledge of the wavelength solution of the ACS grism). While the use of multiple PA’s was quite effective at filtering spurious detections, our tolerance limits and aggressive detection threshold resulted in the detection of fainter emission lines, at the cost of some false-positive detections.

Using the PEARS-2D method allowed us to generate a list of ELR candidates for each PEARS field that did not rely on any pre-generated object catalogs or pre-selection of target galaxies. We stress that a candidate ELR did *not* require the detection of a host galaxy in the field (The fraction of isolated ELR is discussed in Section 3.3). PEARS-2D has three immediate advantages over other methods that rely on observations taken at a single PA: 1) detecting extremely large EWs that would not be identified through more traditional photometric techniques; 2) deriving accurate locations of ELRs without assuming that the source is at the center of the host galaxy, and we can therefore identify multiple ELRs within a single galaxy; and 3) the PEARS-2D line wavelength calibration is significantly more accurate. Normally, the wavelength reference point is tied to the location of the host galaxy (determined using a direct image taken in conjunction with the grism observations). However, since ELRs can be several half-light radii away (amounting to a non-trivial number of pixels). the wavelength solution of the ELR is affected by this distance from the center of the host galaxy. Every error of one pixel in the assumed position of the emission line feature results in a  $40\text{\AA}$  systematic error in wavelength calibration, and therefore a significant redshift error. For large galaxies with multiple ELRs this can lead to errors on the order of several hundred  $\text{\AA}$ . Using the PEARS-2D, this error is avoided because the wavelength solution of the ELRs is determined *independent* of any information about the host galaxy.

### 3.2. Extraction and Verification of Spectra

We extracted spectra of the ELRs candidates identified in Section 3.1 using the PEARS grism data reduction pipeline (e.g. Pirzkal et al. 2009). However, our pipeline was modified, so that we used the positions of the ELRs candidates (i.e. the source of the emission features detected in our grism exposures), rather than a catalog of objects derived from the GOODS broad-band images. The extraction and calibration of the spectra were performed with aXe package (Pirzkal et al. 2001; Kümmel et al. 2009), using optimally weighted spectral extractions and an extraction width of  $3\times$  the measured emission region sizes. Individual spectra were extracted from single ACS grism exposures, and spectra taken at the same PA were then combined using aXeDrizzle (Kümmel et al. 2009). We thus obtained multiple independent spectra for each of our ELR candidate (one per available PA). Wavelength and flux calibration were performed by aXe using the STScI-provided calibration files for the ACS G800L grism. Emission lines fluxes were measured using Gaussian fitting in each extracted spectrum, resulting in 3 to 4 independent measurements. We then computed the average line flux and its associated standard deviation value for each of our emission line candidates. These line fluxes were corrected for Galactic reddening assuming values from Cardelli et al. (1989). The corrections were negligible with  $E(B-V)=0.012$  mag for PEARS-N field and  $E(B-V)=0.0078$  mag for PEARS-S field.

Our list of ELR candidates reached down to very low flux levels, and contained many false positives. We therefore had to vet each ELR and its associated emission line candidates. While we attempted to apply automatic techniques to accept or reject ELR and emission line candidates, we found it useful to manually vet all spectra by eye. Authors of this paper manually examined and graded emission lines on a scale ranging from 0 (very poor) to 5 (very high). Each emission line was graded a minimum of 3 times, and by at least two different persons, and the average of this grade was then adopted. A final grade of 2 was found to correspond to a marginal  $\sim 2\sigma$  detection of spectra obtained in at least two separate PA's. We originally identified a total of 3705 emission-line candidates using the PEARS-2D method described in Section 3.1. The visual quality assessment yielded a sample of 1162 marginally detected emission lines (529 in PEARS-N and 633 in PEARS-S). As multiple emission lines were sometimes detected in an ELR, the final number of ELRs was 985 (451 in PEARS-N and 535 in PEARS-S).

### 3.3. Emission Line & Host Galaxy Identification

Determining the nature of emission lines in the extracted spectra of a given ELR fell into two distinct categories: either multiple emission lines were detected, or only a single

emission line was detected.

The spectral dispersion of the G800L grism is  $\sim 40\text{\AA pixel}^{-1}$  and is too low to resolve and identify close emission line pairs (e.g. [OIII] and  $H\beta$ ). However, in the redshift range of the PEARS survey ( $0 < z < 1.5$ ), there are pairs of widely separated emission lines that allow for both line identification (via the ratio of the observed wavelengths of the two lines) and redshifts to be determined. The line pairs that we considered were: [OII] and [OIII]; [OIII] and  $H\alpha$ ; or CIII] and CIV.

Most of the time spectra contained only one prominent emission line, so we had to rely on a comparison with photometric redshifts of the host galaxy from Dahlen et al. (2010, 2012). While we noted above that the PEARS ELRs were selected independently, we subsequently matched them with a host galaxy in the GOODS fields. We used the public ACS GOODS 2.0 data to generate mosaics of the GOODS fields, and used SExtractor to generate segmentation maps and object catalogs of galaxies for these fields. In the great majority of cases, the RA and Dec of a PEARS ELR clearly fell within the segmentation map of a galaxy. In such cases the corresponding galaxy was assumed to be the host of the ELR, and it was assumed that the redshift of the observed emission lines to be the known photometric redshift for the host galaxy. Some ELRs ( $\approx 6\%$  of objects with a significant emission line with a grade of 2.5 or larger) were found to lie beyond any galaxy segmentation maps. In such cases, the photometric redshift of the GOODS object with the closest segmentation map was used (which is not necessarily the closest object in cases of large extended galaxies). When comparing photometric redshifts to PEARS spectroscopic redshifts obtained using one of the pair of emission lines listed above, in 94% of the cases, the redshifts were within the 95% confidence regions given for the photometric redshifts of Dahlen et al. (2010, 2012). When only a single emission line was detected in a spectrum, it was assumed to be either Ly- $\alpha$ , CIV, CIII], MgII, [OII], [NeIII], [OIII],  $H\gamma$ , or  $H\alpha$ , observed at the assumed GOODS photometric redshift value. We identified the type of the emission line, and computed a spectroscopic redshift for that object simply by selecting the line type that produced the closest match to the observed wavelength.

It should be noted that some of the emission lines discussed in this paper are blended lines, but this should have little effect on our analysis, since weaker lines only weakly bias the fluxes and redshifts that we derive. This is the case, for example, for [OIII] which consists of two unresolved lines at 4959 $\text{\AA}$  and 5007 $\text{\AA}$ ,  $H\alpha$  at 6562 $\text{\AA}$  which is blended with weaker [NII] at 6583 $\text{\AA}$ , while by [NeIII] we actually refers to the stronger component at 3868 $\text{\AA}$ . Furthermore, some for the PEARS ELGs were found to contain more than one ELRs. Since these ELRs and the emission lines their spectra contained were analyzed separately, this provided a way to check the consistency of the PEARS spectroscopic redshifts. In these cases, the redshifts agreed to within  $z = \pm 0.01$ .



As noted earlier, some of the PEARS fields overlap slightly, thus these ELRs were observed and analyzed independently as part of different PEARS fields. Nineteen ELRs were observed twice (15 in PEARS-N and 4 in PEARS-S; the higher number of duplicate observations in PEARS-N is the result of the larger amount of overlapping between individual PEARS-N fields, as shown in Figure 1). Comparing the observed emission lines wavelength, the emission line fluxes, and finally the redshifts, the errors were:  $\langle \delta\lambda \rangle = 18\text{\AA}$ ;  $\langle \frac{\delta f}{f} \rangle = 8\%$ ; and  $\langle \delta z \rangle = 0.003$ , again demonstrating excellent consistency. For the remainder of this paper, we adopt a minimum emission line grade of 2.5 or greater (corresponding to a line flux limit of  $\sim 1 \times 10^{-17}$  erg/s/cm<sup>2</sup>), when deriving properties of H $\alpha$ , [OIII] and [OII] emitters (174, 401, and 167 emission lines, respectively).

### 3.4. Spectroscopic vs. Photometric Equivalent Widths for ELRs at Large Radii

One of the advantages of PEARS-2D is the ability to detect multiple ELRs within a single galaxy (see Figure 2). However, at progressively larger radii from the galaxy center, the contribution from the underlying continuum decreases. Since spectra were extracted at these large radii using small extraction windows, the measured EWs are generally larger than what would be derived by simply comparing the measured line fluxes to the total underlying continuum of the host galaxy. The EWs derived from narrow-band imaging surveys generally rely on the latter method. To quantify any potential differences, photometric EWs ( $EW_{\text{phot}}$ ) were computed using the measured PEARS line flux and the measured total host galaxy broad band flux. On average the spectroscopic EW ( $EW_{\text{spec}}$ ) was  $\sim 3.5 \times (EW_{\text{phot}})$ . Histograms of the  $EW_{\text{spec}}$  values for the H $\alpha$ , [OIII], and [OII] are plotted in Figure 3. We note that for the purposes of this paper an emission line is reported as a positive EW.

### 3.5. Blended Emission [OIII] and H $\beta$ Lines

The ACS G800L grism cannot separate the [OIII] doublet (4959 $\text{\AA}$ , 5007 $\text{\AA}$ ) and H $\beta$  (4681 $\text{\AA}$ ). In this paper, the 4959 $\text{\AA}$ , 5007 $\text{\AA}$  doublet is referred simply to [OIII]. These three lines appear blended in the PEARS spectra, and H $\beta$  can appear as an asymmetric feature to the stronger [OIII] line. To correct the [OIII] fluxes for this effect, each of the lines were fit using separate components. We assumed identical full width at half maximum (FWHM) and assumed a fixed wavelength separation for all three lines. Based on this, we obtained estimates of the [OIII] to H $\beta$  lines ratio for the ELRs. :  $\frac{f(\text{H}\beta)}{f([\text{OIII}])} \approx 0.23 \pm 0.25$ , which is consistent with the relative fluxes expected in star-forming galaxies (e.g., Juneau et al. 2011).

### 3.6. Comparison with Previous PEARS-S Catalog

The PEARS-S data were analyzed and published by Straughn et al. (2009), and are included as part of our analysis of the complete PEARS survey. While our improved analysis reaches down to fainter observed flux-levels, which results in a larger number of ELRs being detected, our emission line list contains in excess of 90% of the emission lines listed in Straughn et al. (2009). However, the number of  $H\alpha$ , [OIII], and [OII] emission lines (with a grade of 2.5 or above) are 1.2, 1.6, and 2.7 times higher, respectively, than in the Straughn et al. (2009) catalog. This is a direct result of our ability to reliably detect fainter emission lines in these data, which particularly affects the intrinsically fainter [OIII] and [OII] emission lines. The use of optimal weighted extraction, as opposed to narrow box extraction (increasing signal-to-noise ratio at the expense of flux completeness, as was the case in Straughn et al. 2009), results in more reliable flux measurements – without a need for an aperture correction – of these emission lines and the lines fluxes measured are on average twice as strong as those listed in Straughn et al. (2009).

### 3.7. Completeness Simulations

Table 4 lists the median and average line fluxes for  $H\alpha$ , [OIII], and [OII] that have a strong detection (PEARS grade of at least 2.5). In Figure 4, we show the distributions of the line fluxes for these three lines. The histograms are plotted as a fraction of the total for each line. Figure 4 demonstrates that the PEARS-2D line fluxes peak at values of  $\sim 10^{-17}$  erg/s/cm<sup>2</sup>. The ACS G800L grism has an approximately flat sensitivity from  $\approx 6000\text{\AA}$  to  $9500\text{\AA}$ , but our ability to recover emission lines from the two dimensional dispersed images needs to be carefully evaluated before we can say anything about our completeness limits and the volume density of these sources. This is particularly important because it must be verified that our sample is not biased by the host galaxy sizes, which vary as a function of redshift (i.e. all lines types are detected equally well). We determined the PEARS-2D detection limits using extensive end-to-end Monte Carlo simulations. These steps are briefly outlined here: First, we started with the real individual PEARS ACS/WFC G800L exposures and artificially added a random distribution of simulated ELRs (and simulated emission lines) to these data. We allowed for a wide ranges of line fluxes, host galaxies, and redshifts in these simulations, and also allowed for random placement of multiple ELRs in each galaxy. Each of the nine PEARS field was simulated ten times, each time adding ELRs to 100 galaxies.

Next, the simulated data were processed and identified using exactly the same procedures used for the real observations. The simulated spectra were then extracted using

aXe, and line fluxes measured, as we described in Section 3.2. Comparing input and output line lists, we found that the PEARS wavelength sensitivity is very similar to the inverse sensitivity of the ACS G800L grism with a sharp cutoff below 5500Å and above 9500Å. This sets the redshift ranges of the PEARS survey for the H $\alpha$ , [OIII] and [OII] lines to be  $0 < z < 0.5$ ,  $0.1 < z < 0.9$ ,  $0.5 < z < 1.5$ , respectively. PEARS was mainly limited by the intrinsic emission line flux, ELRs containing fluxes as low as  $10^{-18}$  erg/s/cm<sup>2</sup> could be detected, and that we could detect more than 85% of emission lines with flux greater than  $\sim 3 \times 10^{-17}$  erg/s/cm<sup>2</sup> and with EW > 50 Å. This is consistent with the observations of observed line fluxes shown in Figure 4. The exact fractions of lines recovered as a function of observed line flux for the PEARS-N, PEARS-S and PEARS-S-HUDF field (which is twice as deep as the other PEARS-S fields) are shown in Figure 5.

### 3.8. Methods for Computing Luminosity Functions and SED Fitting

Here, the methods adopted to determine the PEARS emission line luminosity functions for H $\alpha$ , [OIII] and [OII] are briefly described. We also outline how stellar masses were derived for the ELGs containing the ELRs identified in the previous Sections. Finally, we discuss the different approaches adopted to account for internal dust corrections when computing the PEARS line luminosity functions.

#### 3.8.1. The $1/V_{\max}$ method

This widely used method does not assume a shape for the luminosity function  $\Phi(L)$ . However, one disadvantage is that it requires the data to be binned. The number of bins can impact the results. In this paper, the number of bins was determined using the Freedman-Diaconis rule (Freedman & Diaconis 1981), whereby the bin-size is selected to be  $2 \text{ IQR}(x)n^{-\frac{1}{3}}$ , where IQR is the interquartile range of the data and  $n$  is the number of data points in the sample. Using the  $1/V_{\max}$  method, the luminosity function is computed using the following formula:

$$\Phi(\log L_i) = \frac{1}{\Delta \log L} \sum_j \frac{1}{f(z_j, L_j)V_j} \quad (1)$$

where:  $|\log L - \log L_i| < \frac{1}{2}\Delta \log L$ ;  $\Delta \log L$  is the bin-width;  $V_j$  is the maximum volume within which object  $j$  (observed to have a line flux of  $l_j$  and to be at the redshift of  $z_j$ ) would be detected in our survey; and  $f(z_j, L_j)$  is the incompleteness  $f(l)$  (see Section 3.7),

remapped into absolute luminosity space  $L$  given the object’s redshift  $z_j$ , and is defined as:

$$V_j = \frac{\Omega}{4\pi} \int_{z_{j,\min}}^{z_{j,\max}} \frac{R(z)dV_c(z)}{dz} dz \quad (2)$$

where:  $\Omega$  is the solid angle of our survey (sr);  $V_c(z)$  is the cosmological comoving volume element at redshift  $z$  (in  $\text{Mpc}^3$ ); and  $R(z)$  is the normalized grism response function expressed as a function of object redshift. Given the redshift range  $\{z_l, z_h\}$  at which a given emission line can be observed by the ACS grism (i.e. observed at wavelengths  $6000\text{\AA} < \lambda < 9000\text{\AA}$ ), the minimum redshift,  $z_{j,\min}$  is  $z_l$  while the maximum redshift  $z_{j,\max} = \min(z_h, z_{\text{faint}})$ , where  $z_{\text{faint}}$  is the maximum redshift at which a line with luminosity  $L$  would remain above our minimum line detection threshold  $l_{\text{threshold}}$ . Hence,  $z_{\text{faint}}$  is the redshift corresponding to the distance of  $D_L(z_j)\sqrt{l_j/l_{\text{threshold}}}$ , where  $D_L(z_j)$  is the luminosity distance of object  $j$ .

### 3.8.2. STY method

The STY (Sandage, Tammann, Yahil) method (Sandage et al. 1979) is another commonly used method for estimating the luminosity function. In this one, one assumes that  $\Phi(L)$  has the form of a Schechter function (Schechter 1976):

$$\Phi(L)dL = \Phi_* \left(\frac{L}{L_*}\right)^\alpha \exp\left(-\frac{L}{L_*}\right) \frac{dL}{L_*} \quad (3)$$

which is characterized by the three parameters  $\alpha$ ,  $\Phi_*$ , and  $L_*$ . Following Sandage et al. (1979), the probability of observing a given object  $j$  at redshift  $z$  with a luminosity  $L_j$ , is then:

$$p(L_j, z_j) = \frac{\Phi(L)f(z_j, L_j)R(z_j)}{\int_{L_{\text{faint}}}^{\infty} \Phi(L)f(z_j, L)dL} \quad (4)$$

The joint likelihood can then be computed for the whole group of observed lines:

$$L = \prod_j p(L_j, z_j) \quad (5)$$

From this, can then determine values of  $\alpha$  and  $L_*$  that maximizes this likelihood. The overall normalization constant  $\Phi_*$  cannot be determined this way, because it cancels out in Equation 4. In this paper, we determined the values of  $\alpha$  and  $L_*$  by maximizing Equation 5 using a Monte Carlo Markov Chain approach. This allowed us to determine the most likely

values of these two parameters, as well as 95% credible intervals for these parameters.  $\Phi_*$  was computed by integrating Equation 3 and normalizing the result, so that matched the number of detected objects.  $\Phi_*$  was computed for each combination of  $\alpha$  and  $L_*$  in our Markov Chains to produce 95% credible intervals for the parameter  $\Phi_*$ .

### 3.8.3. Host galaxy SED fitting

Properties of the host galaxies of the PEARS ELRs were estimated by fitting model Spectral Energy Distributions (SEDs) to their broadband photometric colors. The photometric values were taken from the TFIT GOODS measurements (Papovich & Bell 2002), which include 10 and 12 photometric bands in the GOODS-N and GOODS-S, respectively (Laidler et al. 2007; Grogin et al. 2012). The photometry spans the observed UV ( $U$ -band) through thermal-IR based on VLT, *HST* and *Spitzer* observations. The majority (95%) of the PEARS ELGs are detected in the *Spitzer* data and these observations therefore probe the rest-frame optical increasing the robustness of our SED fitting. The actual SED fitting was done using our own Monte Carlo Markov Chain SED fitting code ( $\pi\text{MC}^2$ ) (Pirzkal et al. 2012) to obtain estimates of the stellar masses, extinction, and ages of the host galaxies.  $\pi\text{MC}^2$  is a far more robust method of SED fitting than the standard  $\chi^2$  algorithm because it provides a proper treatment of both error propagation, and a computation of confidence levels. A more detailed explanation of MCMC can be found in (Pirzkal et al. 2012) and references therein.

A simple stellar population model (i.e. single burst) with BC03 (Bruzual and Charlot 2003) templates and a Salpeter IMF were used. While the choice of IMF and input models (e.g. BC03 or Maraston 2005) can affect derived stellar masses, the effects are not the same at all redshifts. The detailed simulations presented in Pirzkal et al. (2012) show that for the redshift range of interest here, stellar mass estimates from different models are consistent with each other to within a factor of a few. The typical uncertainty in our stellar mass estimates is  $\sim 0.25$  dex while the typical uncertainty in our extinction estimates is  $\sim 0.35$ . Other parameters obtained from SED fitting (e.g. extinction, metallicity, and ages of the stellar population) are significantly more uncertain. For the purposes of this paper, we are primarily concerned with stellar mass, and to some extent extinction. In Figure 6, we show the distribution of stellar masses and extinctions for the host galaxies of the PEARS emission line sample. The mean stellar masses of the host ELGs are  $\text{Log}(\text{mass}) = 8.85 \pm 1.03 M_\odot$ . We also estimate that the continuum extinction is relatively low, with an average value of  $A_V = 0.88 \pm 0.92$  mag, listing the  $1\sigma$  dispersion in each case.

### 3.8.4. *Internal Dust corrections to Luminosity Functions*

Using the current PEARS data, there was no way to directly infer the amount of internal (to the host galaxy) dust attenuation affecting the line luminosities. Therefore, three methods were tested for approximating dust corrections to the luminosity functions, and compared to the ones from Ly et al. (2007). The first dust correction used attenuation values from the individual SED fits to the host galaxies. The second method relied on applying an average extinction value of  $A_{H\alpha} = 1.0$  mag (corresponding to  $A_{[OII]} = 1.88$  mag and  $A_{[OIII]} = 1.36$  mag), as is commonly done in SED fitting (e.g., Hopkins 2004; Takahashi et al. 2007). The third method relied on a dust correction based on the somewhat more sophisticated luminosity dependent dust extinction of Hopkins et al. (2001)

While the two first approaches are straightforward, they are a rather coarse attempt at applying dust-corrections. Indeed, these approaches do not allow for the extinction values within ELRs to be different than the host galaxy, and do not allow for the possibility that ELRs might contain a different amount of dust than the host galaxy. The typical nebular extinction is greater than the stellar continuum emission extinction. Applying SED derived extinction values to the PEARS emission lines are therefore likely to be too low (Calzetti et al. 2000). The luminosity dependent approach empirically attempts to circumvent this limitation. In this case, the amount of dust correction is correlated with the measured line luminosities. This method, unlike the first two, could in principle affect the shape of the luminosity functions. We implemented the luminosity correction following the equations listed in Hopkins et al. (2001) and re-deriving equation 5 therein for the specific wavelength of either  $H\alpha$ ,  $[OII]$ , or  $[OIII]$ .

However, the three methods of correcting for dust have only limited effect on the resulting luminosity functions. They simply shift the luminosity functions by a fixed amount without affecting the slope ( $\alpha$ ) at all (as is the case when using the first two methods), or only alter the slope ( $\alpha$ ) slightly (as is the case when applying a luminosity dependent dust-correction). As expected, the  $[OII]$  lines were more affected by dust than the  $[OIII]$  and  $H\alpha$  lines. However, in total, for  $H\alpha$ ,  $[OIII]$  and  $[OII]$  the slopes varied by only  $\sim 0.1$  on average, using either of the three methods discussed above. Hence, we conclude that the effect of dust correction on the slope of the luminosity functions is therefore negligible to within the statistical fitting error in  $\alpha$ .

## 4. Results

### 4.1. The Emission Line Regions

#### 4.1.1. Star-Forming Galaxy Density

Using the uncorrected PEARS lines listed in Table 4, we can compute a space density of star-forming galaxies (SFGs) — as measured by the PEARS survey — and compare it to previous ACS grism based surveys. The star-forming galaxy density at  $0.3 < z < 1.3$  is estimated to be  $4.5 \times 10^{-3} \text{ Mpc}^{-3}$ . This is in complete agreement with previous ACS grism pure parallel surveys, such as the one described in Drozdovsky et al. (2005).

#### 4.1.2. Luminosity Functions

We computed the luminosity functions for our  $\text{H}\alpha$ , [OIII], and [OII] samples, using both the  $1/V_{\text{max}}$  method and the STY methods described in Sections 3.8.1 and 3.8.2. The luminosity functions presented are for ELGs and not simply ELRs. We computed an integrated line luminosity for each galaxy by summing up the contributions from all ELRs in each galaxy. The non dust-corrected luminosity functions, computed using the  $1/V_{\text{max}}$  method, are shown in Figures 7 to 9. In these figures, the new measurements are compared to those of Ly et al. (2007), shown with open triangles and also uncorrected for dust. One additional constraint to the data from Ly et al. (2007) was added, namely that the comparisons were made only with objects with EWs  $> 50\text{\AA}$ .

The results from PEARS agree fairly well with earlier results, although PEARS probes lower line luminosities for [OIII] and  $\text{H}\alpha$ . The  $1/V_{\text{max}}$  results from PEARS-N and PEARS-S are plotted separately in Figures 7 to 9. The differences between these two large and independent fields are well within the statistical errors. Table 5 summarizes the results from fitting the luminosity functions to each of the emission lines in each field separately, as well as PEARS-N and -S together using both the  $1/V_{\text{max}}$  and STY methods. Table 5 also includes the associated 95% credible intervals.

When using the  $1/V_{\text{max}}$  method, as noted in Section 3.8.1, the choice of bin size is important. We illustrate the effect of various bin sizes by showing (using light shaded circles) the luminosity functions that we compute while allowing the bin sizes to vary. As one can see, the effect of bin size has an immediate effect on the values that we derive at a given luminosity. The luminosity derived with the optimal bin sizes is shown using solid symbols. The error bars associated with individual points were derived using a few thousands bootstrapping iterations.

Here, we note that the STY method produces slightly different luminosity function slopes than  $1/V_{\text{max}}$  for [OII], although the two methods are consistent with each-other. The differences between the two are likely due to the limited number of sources over a wide redshift range. This underlines the difficulties in obtaining luminosity function estimates from a limited numbers of sources, as well as the impact of using different methods.. The results shown in Figures 7 to 9 are also in general consistent with those of Ly et al. (2007). The fraction of AGN in our sample is low. Comparing our catalog to x-ray detected sources in the GOODS areas (Alexander et al. 2003), we estimate that AGN contamination is  $\sim 3\%$ .

#### 4.1.3. *The Spatial Distribution of ELRs*

A major difference between PEARS-2D and other ELG studies is that we are able to detect the presence of multiple ELRs within a single galaxy. A breakdown of the sample shows that 69% of the ELGs contain a single ELR; 24% contain two ELRs; 4% contain three ELRs; and 3% contain four or five ELRs. Comparing the location of these ELRs, as parametrized by their distance to the center of the host ELG normalized by the half-light radius ( $R_{hl}$ ) of the host ELG, allows us to compare the distribution of single emission-line regions to the distribution of multiple emission-line regions. Figure 10 shows that there is no indication of any strong differences between the two samples. In both cases, the emission-line regions appear to be predominantly located around one half-light radius away from the center of the ELG. A Kolmogorov-Smirnof test (KS) p-value of 0.49 was computed, which fails to demonstrate that these distributions are statistically different.

#### 4.1.4. *Star Formation Rates of ELGs*

Assuming that ELGs are representative of star-forming galaxies in general, the depth of the PEARS-2D study and large contiguous redshift range allows us to address the relationship between SFR and redshift. The SFR was calculated for the [OII] and  $H\alpha$  emission lines using the Kennicutt (1998) relations. For [OIII] lines, which are likely to be blended [OIII] and  $H\beta$  lines, the relation from Equation 5 in Drozdovsky et al. (2005) was adopted to correct for contamination. We note that while [OIII] emitters cover the broadest redshift range in our sample, [OIII] is the least reliable SFR indicator, especially since we unable to account for the metallicity of each source. The results are shown for individual ELR as a function of redshift in Figure 11. Also plotted (as solid lines) is the SFR for emission lines with an observed flux of  $1 \times 10^{-17}$  erg/s/cm<sup>2</sup>. This illustrates our ability to detect emission-lines uniformly from  $0 < z < 1.5$ .



To analyze the growth of stellar mass in galaxies, it is useful to normalize the computed total galaxy SFRs – summing up contributions from different ELR when necessary – by the galaxies’ stellar masses computed in Section 3.8.3. The resulting specific SFR (sSFR) allows a comparison of all galaxies’ SF activity, in units of the time it would take to build the current stellar mass at their current SFR. A histogram of the dust corrected sSFR for the PEARS-2D ELGs is shown in Figure 12. The dust corrections were derived using the luminosity dependent dust extinction from Hopkins et al. (2001) discussed in Section 3.8.3. Because the dust corrected sSFR value of a galaxy can be considered as one build-up over the life time of a galaxy — assuming constant star-formation rate — the PEARS ELGs sSFRs imply a possible stellar mass built-up time of a few billions years. Note, however, that these sSFR estimates should be considered lower limits since some non-detected star formation might be present in the PEARS ELGs.

There has been some discussion (e.g., Guo et al. 2011) as to whether the SFR in star-forming regions of galaxies should be spatially correlated with the star-forming regions within the galaxy. We investigate this possible relation using the PEARS ELG sample. Figure 13 shows a plot of the estimated SFR of each ELR in the PEARS-2D sample, separating  $H\alpha$ , [OIII] and [OII] emitting regions as a function of radial distance of the ELR (normalized to the continuum half light radius of the galaxy). As this Figure shows, there is no indication for trends as a function of ELR-location for either one of the three types of ELGs examined. A simple Pearson’s linear correlation test for  $H\alpha$ , [OIII] and [OII] yields values of  $-0.03$ ,  $-0.03$  and  $-0.01$ , respectively, indicating no statistical correlation between the location of ELRs and SFR from those ELRs.

Finally, Figure 14 compares dust-corrected SFR against  $M_*$  for the ELGs in the PEARS-2D sample (open circles in all panels). The ELGs are plotted in four redshift bins to match the results of Noeske et al. (2007). In that work, Noeske et al. (2007) derived a “main-sequence” of star-forming galaxies for field galaxies in the Extended Groth Strip, complete to  $\text{Log } M \sim 10.8$  (Figure 1 in that paper). The red squares in Figure 14 are the median values for the galaxies of Noeske et al. (2007), along with the  $\pm 1\sigma$  (dotted red line). Their conclusion was that there exists a gradual decline in SF of most galaxies since  $z \sim 1$ . The implication is that the same physics that regulates SF in local disk galaxies is occurring at  $z \approx 1$ , which could be either due to an evolution in the gas supply or changes in the SF efficiencies. Noeske et al. (2007) suggested that the slope of their star-formation “main-sequence” is related to the gas-exhaustion of galaxies, and is related to the age of the galaxy and its star-formation timescale, all of which are dependent on the galaxy mass. The PEARS-2D sample probes galaxies to much lower masses than those in Noeske et al. (2007). The PEARS galaxies are compared to those in Noeske et al. (2007) in Figure 14. Our results suggest that the “main sequence”, previously found for more massive galaxies, exists down to very low stellar masses,  $\sim 10^8 M_\odot$ , out to  $z \sim 1$ . There is also potentially a flattening of the sSFR

versus mass relation for lower mass objects (i.e., below  $\approx 10^8 M_\odot$ ). The slope of the "main sequence" can differ for different SFR indicators. However, such a flattening in SFR vs. stellar mass, if real, would indicate an even steeper increase of sSFR with decreasing stellar mass than Noeske et al. (2007b) had found at higher masses, and aggravate the requirement for a late onset of efficient SF in low mass galaxies, discussed by these authors. The dashed horizontal lines in Figure 14 show our sensitivity limits at the lower and higher ends of the redshift ranges shown. It is clear that the flattening of this relation is not caused by incompleteness, especially at the higher redshifts.

## 4.2. The Host Galaxies

### 4.2.1. Morphologies

The PEARS-2D galaxies comprise a remarkably robust sample to test the evolution of ELGs and compare their morphologies with physical properties such as SFRs and stellar masses. Unlike many morphological studies, our sample was not pre-selected by redshift or luminosities. The PEARS sample was found to be mostly unbiased by the actual morphology of the host galaxies. It should be noted, however, that the PEARS sample is dependent on the strength of emission-lines and would therefore tends to favor the inclusion of low extinction and low metallicity galaxies. In this section, we parameterize the morphologies of the host galaxies using the Gini Coefficient  $G$  and  $M_{20}$  parameters (Lotz 2004). The  $G$  and  $M_{20}$  parameters can be thought of as proxies for clumpiness and concentration coefficients, respectively, and have been shown to be a good way to distinguish between "normal" galaxies and galaxy mergers in the local Universe (Lotz 2004) in the blue using the Sloan  $B_J$ , Thuan-Gunn  $g$ , and  $B$ -bands to classify local normal galaxies and rest-frame R-band for all types of mergers. Local spiral and elliptical galaxies follow a well defined  $G$ - $M_{20}$  sequence (e.g. Figure 9 in Lotz 2004)), while mergers have larger  $G$  and smaller  $M_{20}$  values (Lotz 2004, 2008, 2010). In order to compare the PEARS ELGs to galaxies in general, we computed the rest-frame  $G$  and  $M_{20}$  coefficients for both the PEARS ELGs as well as the entire GOODS catalog using the public GOODS V2.0 ACS data. These values were measured in all available observed wavelengths, and a rest-frame  $\lambda \sim B$ -band (or  $\sim 4350 \text{ \AA}$ ) value was obtained by linearly fitting these measurements.

As a comparison, field galaxies from the same GOODS fields are included using the public GOODS V2.0 ACS data. For these objects, photometric redshifts were used to derive rest frame B-band values for  $G$  and  $M_{20}$ . The rest-frame values of  $G$  and  $M_{20}$  were computed by linearly fitting the values measured in each of the available bands. The galaxies are all plotted in Figure 15, which is divided into three rows of three panels for clarity. The field

galaxies from GOODS are plotted as contours, and in each panel the  $H\alpha$  [OIII], and [OII] ELGs are shown separately. The solid lines in Figure 15 delineates disturbed galaxies (above the line) from "normal" galaxies (below the line), following to Lotz (2004). Also shown are the regions containing early-type and late-type "normal" galaxies. When compared to the rest of the GOODS field galaxies (black contours), the PEARS ELGs clearly have higher  $G$  and  $M_{20}$  values, and fall above the fiducial line separating quiescent galaxies from active galaxies (following Lotz 2004). This strongly suggests that the PEARS ELGs have perturbed morphologies. While it is possible that some, most, or even all of the PEARS host galaxies are ongoing mergers, it is difficult to quantify without similar  $G$  and  $M_{20}$  measurements of mergers using restframe B-band imaging. We note that in Lotz (2004, 2008), the mergers were predominantly Ultraluminous Infrared Galaxies (ULIRGs) in various stages of interaction (i.e. ranging from two discernible progenitors to single objects with coalesced nuclei) and were based on observations obtained with the  $F814W$  filter using WFPC2 on *HST*. The median redshift of this heterogeneous sample placed the observations at  $\sim$  rest-frame  $R$ -band. As noted in Taylor-Mager et al. (2007); Rothberg & Fischer (2010); Rothberg et al. (2013) the structure and morphology of mergers change as a function of wavelength from UV to near-IR. Moreover, the stage of the merger can affect concentration indices (Taylor-Mager et al. 2007). At best, we can state that the PEARS sample is dominated by clumpy systems dis-similar to nearby normal galaxies at rest-frame  $B$ -band and *may* indicate some type of merger activity is occurring for some of the sample.

There is an indication that ELGs with more than one detected ELR tend to have more disrupted morphologies, while ELGs with a single ELR tend to lay closer the the line separating normal galaxies and mergers (bottom three panels), as defined by Lotz (2004). However, there is no correlation between the Gini- $M_{20}$  values and their computed SFRs and stellar masses. To test for any correlation correlation, the Pearson Correlation coefficient ( $r$ ) was used. It tests the degree of linear correlation between two independent data sets. Here,  $r$  ranges in value from  $-1$  to  $+1$  (perfect negative or anti-correlation to perfect positive correlation). The most correlated relation we find is that of the [OIII] versus stellar mass, shown in Figure 16, which which shows a very weak with a value of  $r = 0.16$ . All other relations show no statistically significant correlation.

#### 4.2.2. $4350\text{\AA}$ Rest-frame Luminosity of ELGs

The underlying host galaxy luminosity may provide additional information about the nature of the ELGs, and how they compare to other galaxies in the field. Rest-frame absolute magnitudes at  $4350\text{\AA}$  ( $M_{4350}$ ) were computed for both the ELGs and the GOODS field galaxies. Figure 17 shows a histogram distribution of  $M_{4350}$  for the ELGs, divided into three

panels — one for each emission line. The median  $M_{4350}$  values for each emission line are:  $-21.2$  mag for [OII];  $-19.0$  mag for [OIII]; and  $-18.2$  mag for  $H\alpha$ .

One important question is whether the ELGs are representative of other galaxies within the same volume. As discussed in the Introduction, ELGs are very useful for probing the evolution of the SFR, not only out to more distant epochs, but also to fainter luminosities (and thus lower masses) than other galaxies. Figure 18 compares the luminosity function of the ELGs — separated by emission line which sample different redshift bins — that form stars strongly enough to be detected at all redshifts in the PEARS sample. Our survey line sensitivity limit of  $3 \times 10^{-17}$  erg/s/cm<sup>2</sup> corresponds to an SFR of  $6 M_{\odot}yr^{-1}$ , at the maximum redshift of  $z \sim 1.5$  that is probed by PEARS. This SFR is in between the values observed in a strong star forming galaxy such as M51 (NGC 5194), with an SFR of  $\sim 3.5 M_{\odot}yr^{-1}$  (Calzetti et al. 2005), and the SFR of starburst galaxies such as M82 with an SFR of  $10 - 30 M_{\odot}yr^{-1}$  (Beswick et al. 2006). In Figure 18, the line luminosity function is plotted for these star forming galaxies and compared to the the luminosity function of the GOODS field galaxies. While the luminosity functions of the GOODS field galaxies increase monotonically in a power law manner, the volume density of strong line-emitters decreases quickly in the redshift bin  $0.5 < z < 1.5$  for host galaxies with  $M > -20$  mag. The GOODS data are faint enough to detect host galaxies that are much fainter ( $M \sim -15$  mag). The PEARS survey is sensitive enough to detect the emission lines from such strong star forming galaxies, but we did not identify emission lines galaxies with  $M > -18$  mag in the higher redshift range of the survey. It is unlikely that this apparent decrease is caused by incompleteness because the sample is restricted to include only objects with line fluxes that are comfortably above the incompleteness limit and, as long as a galaxy forms stars at a rate greater than  $6M_{\odot} yr^{-1}$ , this will result in an emission line that is bright enough to be detected and identified by the PEARS-2D method. The PEARS survey might simply be missing galaxies at higher redshifts if these objects are intrinsically more dusty at higher redshift, but the required amount of extinction are large and we see not evidence for an increase in the SED derived extinction for the objects we detect, as a function of redshift.

We can also quantify any redshift dependence of the volume density of line-emitting galaxies by examining the volume densities of just the [OIII] emitting galaxies at redshifts from  $z \approx 0.1$  to  $z \approx 0.9$ . This is the redshift range with the largest number of ELGs and [OIII] lines should be less sensitive to dust than the [OII] lines discussed above. When examining the [OIII] line emitters, we now restrict our sample to galaxies with  $SFR > 1.7M_{\odot}yr^{-1}$ , our SFR completeness limit at  $z = 0.9$ , which is smaller than the limit we used when we included the [OII] ELGs, but still select galaxies with robust star formation – while maintaining a sample size that is as large as possible. The [OIII] host galaxy sample was divided into two distinct redshift ranges ( $0.1 < z < 0.5$  and  $0.5 < z < 0.9$ ) and the results are plotted in Figure

19. This Figure shows the luminosity functions as a function of both  $M_{4350}$  (*left*) and Stellar Mass (*right*). The left panel of Figure 19 confirms that there appears to be a relatively small number of faint galaxies with detected [OIII] emission at higher redshifts. Recall that these host galaxies were selected solely based on the direct and independent detection of [OIII] in emission, and thus were selected independently of their observed size and host luminosity.

In the right panel of Figure 19, the stellar masses are compared for the two redshift ranges (same limits on sample selection as in the left panel). The stellar mass distribution of galaxies with detected [OIII] emission differs significantly. At lower redshift there appears to be fewer massive galaxies with detected star-formation  $> 1.7M_{\odot}yr^{-1}$ . We conclude that the ratio of star-forming massive galaxies to passive massive galaxies is higher at high redshift, which is a result that is consistent with downsizing (e.g., Cowie et al. 1996).

## 5. Conclusions

We have presented a sample of ELGs selected independently by their emission-lines without *a priori* knowledge of their host galaxies properties. The methodology used (PEARS-2D) is based on *direct* detection of emissions-line from *HST* slitless grism spectroscopy, with the added bonus of being able to detect multiple ELRs within a single galaxy. This has yielded a sample, which is effectively random and blind to other parameters. Using the wealth of ancillary data, the properties of the underlying host galaxies were compared with the SFR histories derived from the ELRs. The key results are summarized below:

- 1) There is evidence for evolution in the luminosity functions of the  $H\alpha$ , [OIII] and [OII] emission lines. The luminosity function slopes flatten as a function of redshift.
- 2) The morphology of the host galaxies clearly indicates that these objects are clumpy, although we detect no correlation between their morphology and our stellar mass estimates or star-formation intensity (sSFR).
- 3) The mass-density function of [OIII] emitting galaxies at  $0 < z < 0.9$  strongly decreases with redshift. The number density of objects with stellar masses greater than  $\sim 10^{10} M_{\odot}$  undergoing strong star-formation decreases at lower redshifts. This supports the idea of galaxy downsizing (Cowie et al. 1996, e.g.).

The results presented here also demonstrate the clear advantage of space-based grism spectroscopy using multiple position angles. Such observations are able to probe deeper than similar ground-based studies. The PEARS-2D method also provides a method for detecting multiple ELRs, and allows spatial information about SF to be derived for galaxies. Future work will include using the WFC3 near-IR grism mode, with observed wavelength coverage of 0.8-1.6 $\mu$ m. This will allow us to probe to significantly higher redshifts, and determine whether the trends reported here continue to earlier epochs. After 2018, this work can also

be done at much higher sensitivities with the JWST FGS grism at  $1 - 2\mu m$ , and the JWST NIRcam prisms at  $2.5 - 5\mu m$ .

*Acknowledgments* - NP wishes to thank F. Pierfederici for his help during the preparation of this manuscript. This research made use of the OSX version of SCISOFT assembled by Dr. Nor Pirzkal and F. Pierfederici.

Pre-print

.tex

.tex

Pre-print

Table 1. Summary of emission lines detected in the PEARs survey using the PEARs-2D method.

PEARs Field	R.A.	Dec.	No. PA <sup>a</sup>	Exposure (s) <sup>b</sup>	No. Objects	No. Knots	No. of lines										
							[OII]	[OIII]	H $\alpha$	CIV	CIII]	MgII	[NeIII]	H $\gamma$	Ly- $\alpha$	noID	All <sup>c</sup>
PEARs-N-1	189.1852503	+62.2032822	3	44708	153	167	48	73	26	5	6	6	1	5	2	1	173
PEARs-N-2	189.1877163	+62.2548588	3	44252	90	96	29	50	15	1	4	3	4	4	1	5	116
PEARs-N-3	189.3100669	+62.2924237	3	44708	98	104	33	43	16	5	9	5	1	2	1	2	117
PEARs-N-4	189.3720309	+62.3201389	3	44708	91	98	23	42	35	1	10	3	0	2	1	6	123
PEARs-S-HUDF	53.16231255	-27.7911063	4	89819	152	166	46	61	40	7	7	13	0	3	2	14	193
PEARs-S-1	53.16967450	-27.9014641	3	43733	54	61	10	34	28	0	0	0	0	2	0	2	76
PEARs-S-2	53.17745315	-27.8416506	4	51583	52	54	20	40	5	0	0	0	1	2	0	2	70
PEARs-S-3	53.11987485	-27.7396665	3	44186	112	127	29	59	34	0	6	5	1	3	1	7	145
PEARs-S-4	53.06664343	-27.7088154	4	44084	123	131	31	62	20	3	4	9	2	6	3	9	149
PEARs-N <sup>d</sup>					417	451	133	208	92	12	29	17	6	13	5	14	529
PEARs-S <sup>e</sup>					489	535	136	256	127	10	17	27	4	16	6	34	633
PEARs TOTAL <sup>f</sup>					906	986	269	464	219	22	46	44	10	29	11	48	1162

Note. — (a) Number of HST orientations at which this field was observed.

(b) Total exposure time (in s) of all the data obtained for this field, including all orientations.

(c) Includes Ly- $\alpha$ , CIV, CIII], MgII, [OII], [NeIII], [OIII], H $\gamma$ , and H $\alpha$ .

(d) Sum for all the PEARs-N fields.

(e) Sum for all the PEARs-S fields.

(f) Sum for all of the PEARs fields.

(g) Sum for all of the PEARs fields.



Table 2. Properties of PEARs Emission-Line Galaxies.

PEARs Field	PEARs ID	PEARs ELR ID	R.A. (deg)	DEC (deg)	Grism Redshift	Flux ( $10^{-18} \text{ erg/s/cm}^2$ )	Wavelength ( $\text{\AA}$ )	EW ( $\text{\AA}$ )	$i_{AB}$ (mag)	Line ID	Line Grade
PEARs-N-1	n30256	1	189.18592310	62.16982753	0.94	$26.1 \pm 1.9$	7217	80	23.7	[OII]	3.8
PEARs-N-1	n30256	1	189.18592310	62.16982753	0.94	$137.0 \pm 18.0$	9710	363	23.7	[OIII]	3.1
PEARs-N-1	n31345	1	189.16498516	62.17099244	0.49	$39.8 \pm 12.1$	7437	194	26.1	[OIII]	3.3
PEARs-N-1	n33944	1	189.16105015	62.17608778	0.69	$62.9 \pm 3.8$	8454	223	24.1	[OIII]	3.7
PEARs-N-1	n35090	1	189.20037133	62.17725706	0.65	$26.0 \pm 2.4$	8237	212	24.4	[OIII]	4.0
PEARs-N-1	n35767	1	189.20747927	62.17882730	0.48	$16.3 \pm 15.2$	7344	107	25.0	[OIII]	3.0

Note. — This table is available in its entirety in the online journal. A portion of it is shown here.

Table 3. Luminosity Function

Method	Line	Redshift Range	PEARS-N		PEARS-S		PEARS		
			$L_*$	$\alpha$	$L_*$	$\alpha$	$L_*$	$\alpha$	$\Phi_*$
STY	OII	$0.5 < z < 1.6$	$41.45^{+1.56}_{-0.14}$	$-1.23^{+0.42}_{-0.87}$	$41.95^{+0.48}_{-0.48}$	$-1.49^{+0.53}_{-0.35}$	$41.75^{+0.57}_{-0.29}$	$-1.44^{+0.38}_{-0.42}$	$-4.63^{+0.52}_{-4.66}$
	OIII	$0.1 < z < 0.9$	$41.65^{+0.57}_{-0.12}$	$-1.23^{+0.14}_{-0.21}$	$41.68^{+0.36}_{0.00}$	$-1.19^{+0.10}_{-0.23}$	$41.67^{+0.10}_{-0.13}$	$-1.21^{+0.11}_{-0.12}$	$-3.45^{+0.21}_{-0.42}$
	H $\alpha$	$0.0 < z < 0.5$	$41.01^{+0.43}_{-0.22}$	$-1.14^{+0.26}_{-0.29}$	$40.83^{+0.01}_{-0.24}$	$-0.86^{+0.29}_{-0.18}$	$40.90^{+0.07}_{-0.03}$	$-0.97^{+0.11}_{-0.19}$	$-2.72^{+0.16}_{-0.43}$
$1/V_{\max}$	[OII]	$0.5 < z < 1.6$	$44.46^{+0.54}_{-0.14}$	$-1.84^{+0.11}_{-0.15}$	$44.35^{+0.65}_{-1.61}$	$-1.93^{+0.12}_{-0.10}$	$43.24^{+1.76}_{-1.07}$	$-1.93^{+0.14}_{-0.08}$	$-5.49^{+1.24}_{-1.99}$
	[OIII]	$0.10 < z < 0.90$	$40.87^{+0.07}_{-0.13}$	$-0.77^{+0.23}_{-0.10}$	$41.45^{+0.21}_{-0.17}$	$-1.19^{+0.15}_{-0.12}$	$41.31^{+0.09}_{-0.09}$	$-1.21^{+0.08}_{-0.07}$	$-2.58^{+0.09}_{-0.09}$
	H $\alpha$	$0.00 < z < 0.49$	$40.89^{+0.13}_{-0.17}$	$-1.10^{+0.13}_{-0.11}$	$41.42^{+0.44}_{-0.26}$	$-1.45^{+0.06}_{-0.10}$	$41.01^{+0.06}_{-0.09}$	$-1.24^{+0.05}_{-0.04}$	$-2.47^{+0.07}_{-0.07}$

Pre-print

Table 4. Properties of significantly detected (grade>2.5) emission lines in the PEARS sample

Line	Number Detected	$\langle z \rangle$	Flux (erg/s/cm <sup>2</sup> )	
			Average	Median
H $\alpha$	174	0.26	$9.44 \times 10^{-16}$	$5.54 \times 10^{-17}$
[OIII]	401	0.54	$9.65 \times 10^{-17}$	$4.13 \times 10^{-17}$
[OII]	167	0.91	$4.19 \times 10^{-17}$	$2.49 \times 10^{-17}$

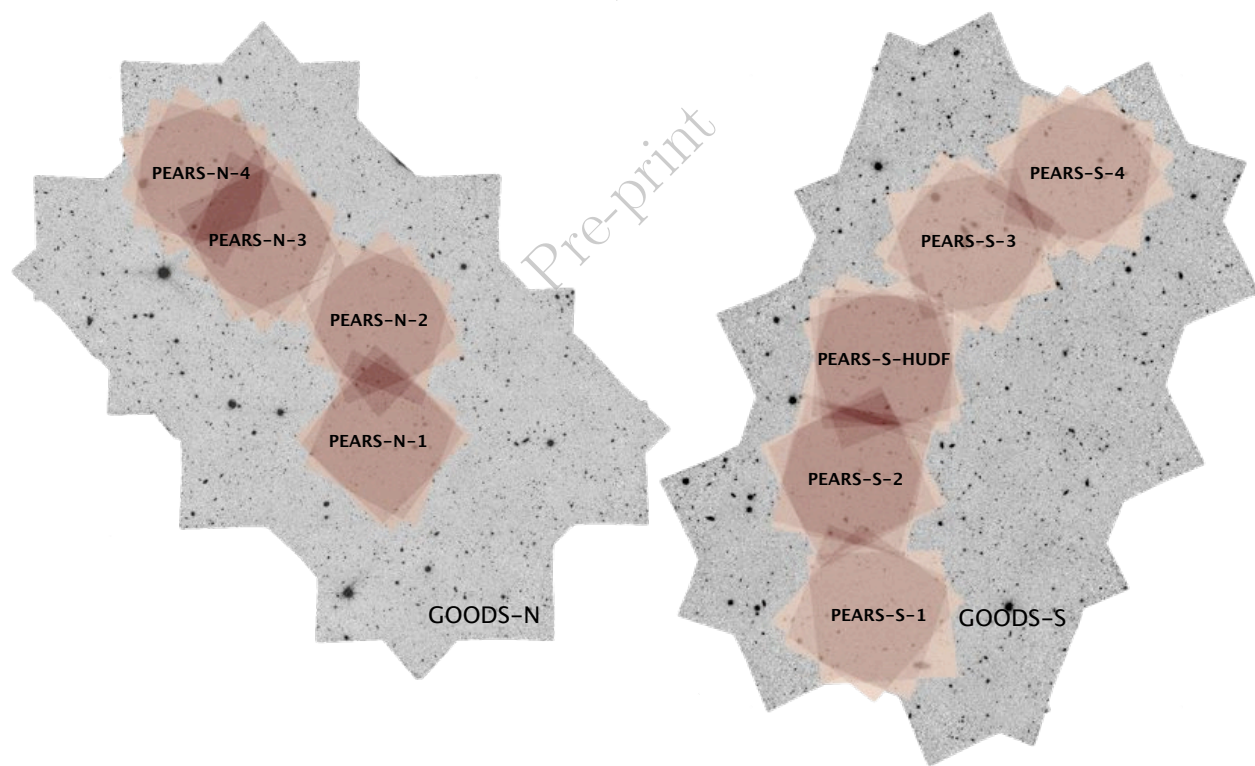


Fig. 1.— The location of the four PEARS-N (left) and five PEARS-S pointings (right) within the GOODS-N and GOODS-S fields. The fields are oriented so that North is up and East is to the left. Each of the shown PEARS fields is approximately 200'' arc second wide. Note that the total area where PEARS fields overlap is somewhat higher in PEARS-N than in PEARS-S.

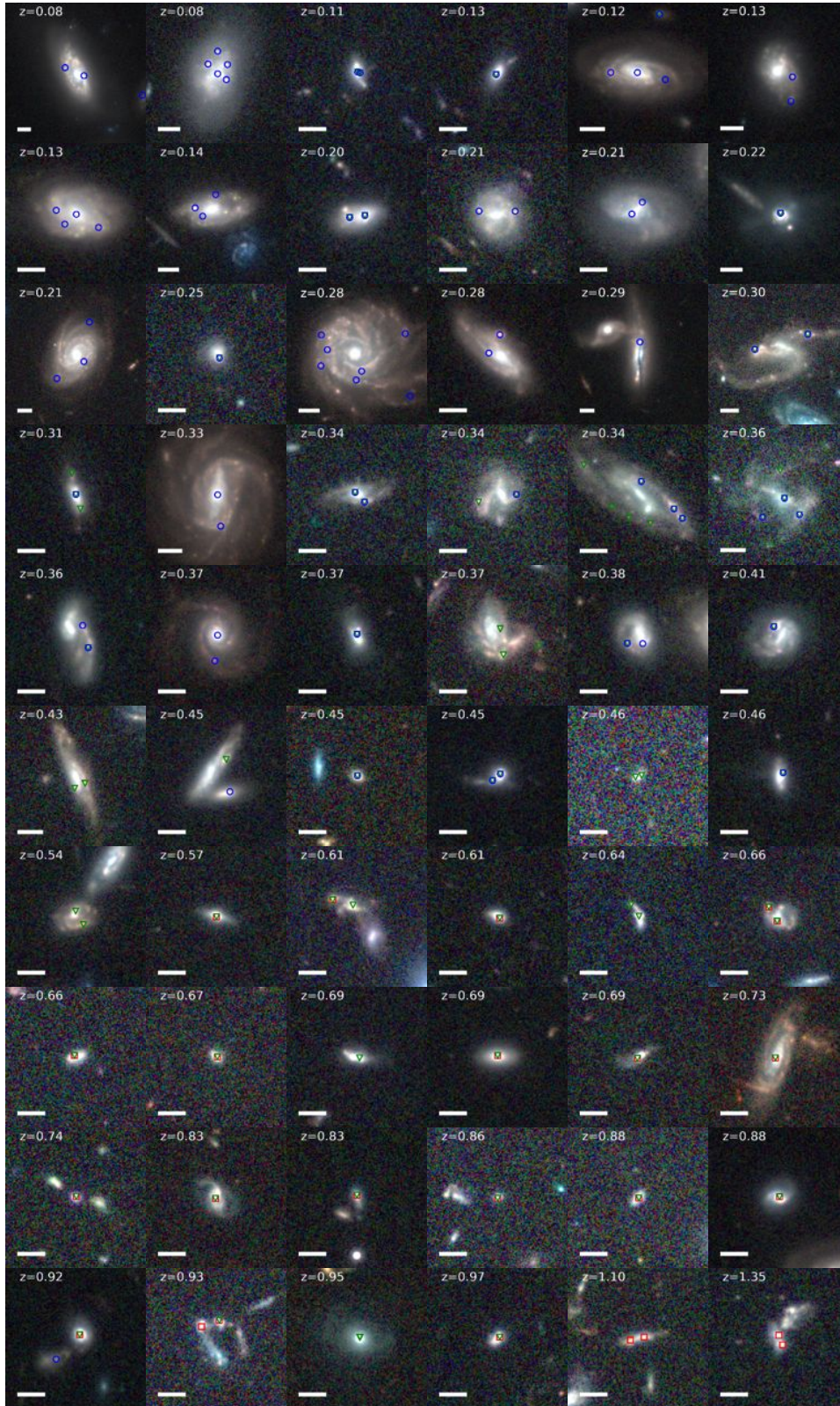


Fig. 2.— A sample of PEARS star-forming galaxies with their identified star-forming regions by red squares ([OII]), green triangles ([OIII]), and blue circles ( $H\alpha$ ). The redshift is indicated at the top-left of each stamp image, and the one arc second scale is shown at the bottom-left of each stamp image.

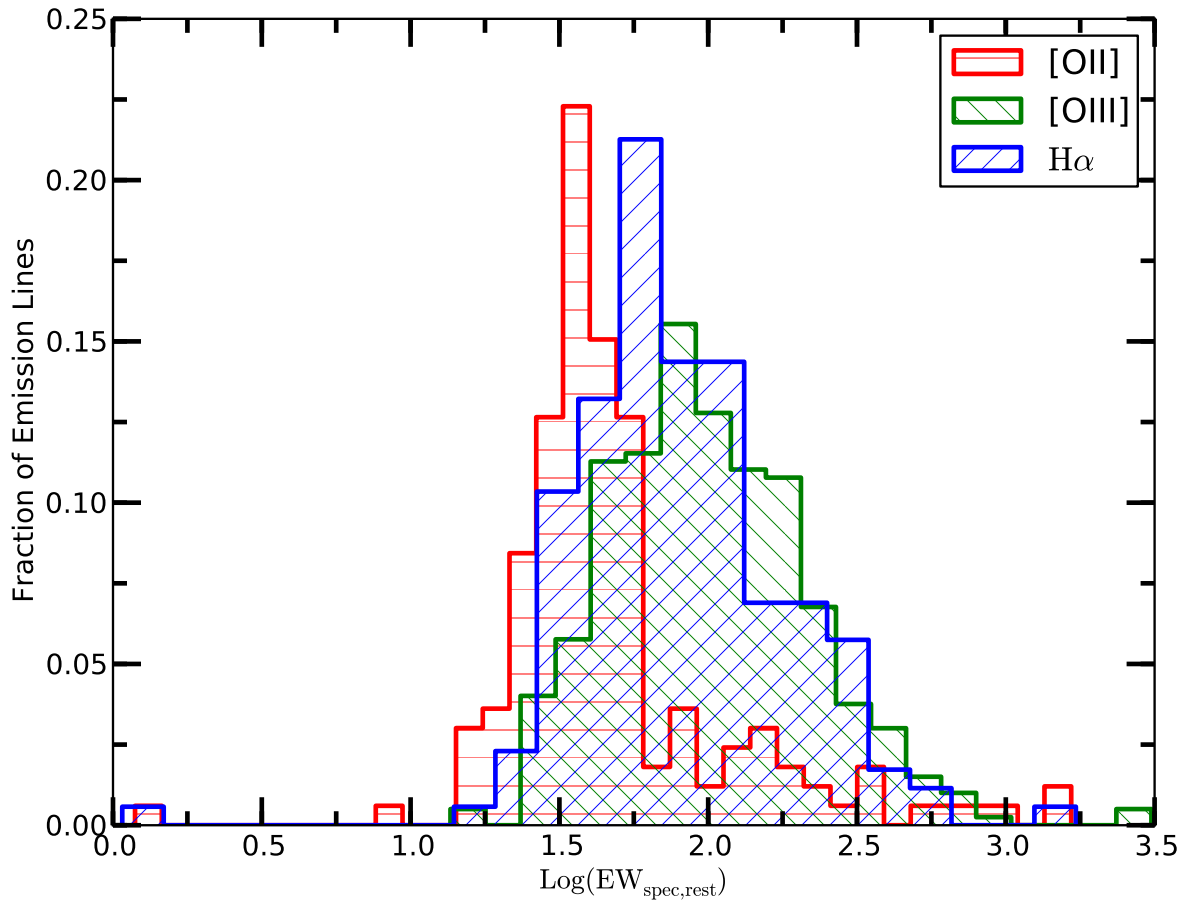


Fig. 3.— Rest-frame spectroscopic EWs of the PEARS-2D sample for emission-lines with a grade greater than 2.5. The median  $\text{EW}_{\text{spec}}$  we measured are  $39\text{\AA}$ ,  $91\text{\AA}$ , and  $71\text{\AA}$  for [OII], [OIII], and  $\text{H}\alpha$  emission lines, respectively. These lines act as proxies for the redshift ranges of  $0 < z < 0.5$ ,  $0.1 < z < 0.9$ , and  $0.5 < z < 1.5$ , respectively.

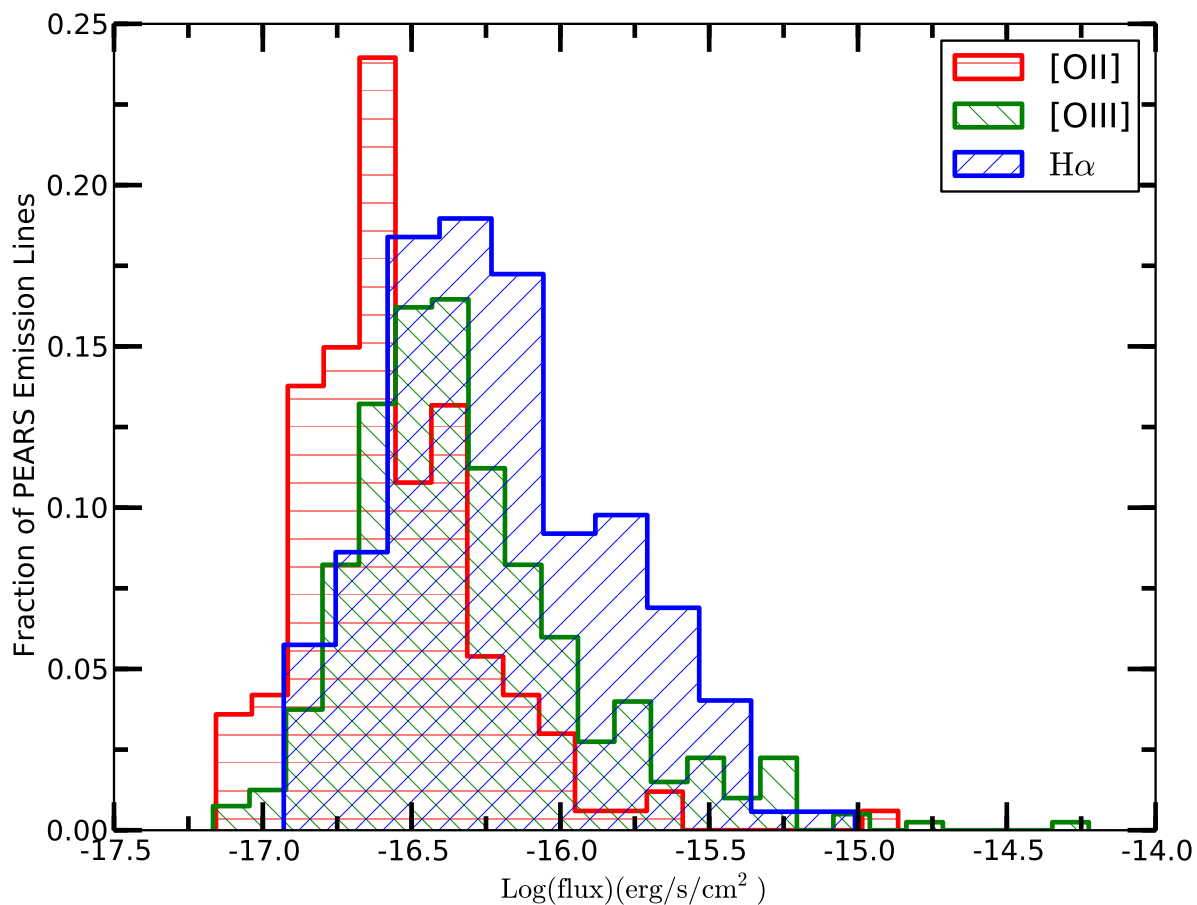


Fig. 4.— Distributions of observed line fluxes in the PEARS-2D sample for emission-lines with a grade greater than 2.5, uncorrected for completeness or dust extinction. These lines act as proxies for the redshift ranges of  $0 < z < 0.5$ ,  $0.1 < z < 0.9$ , and  $0.5 < z < 1.5$ , respectively.



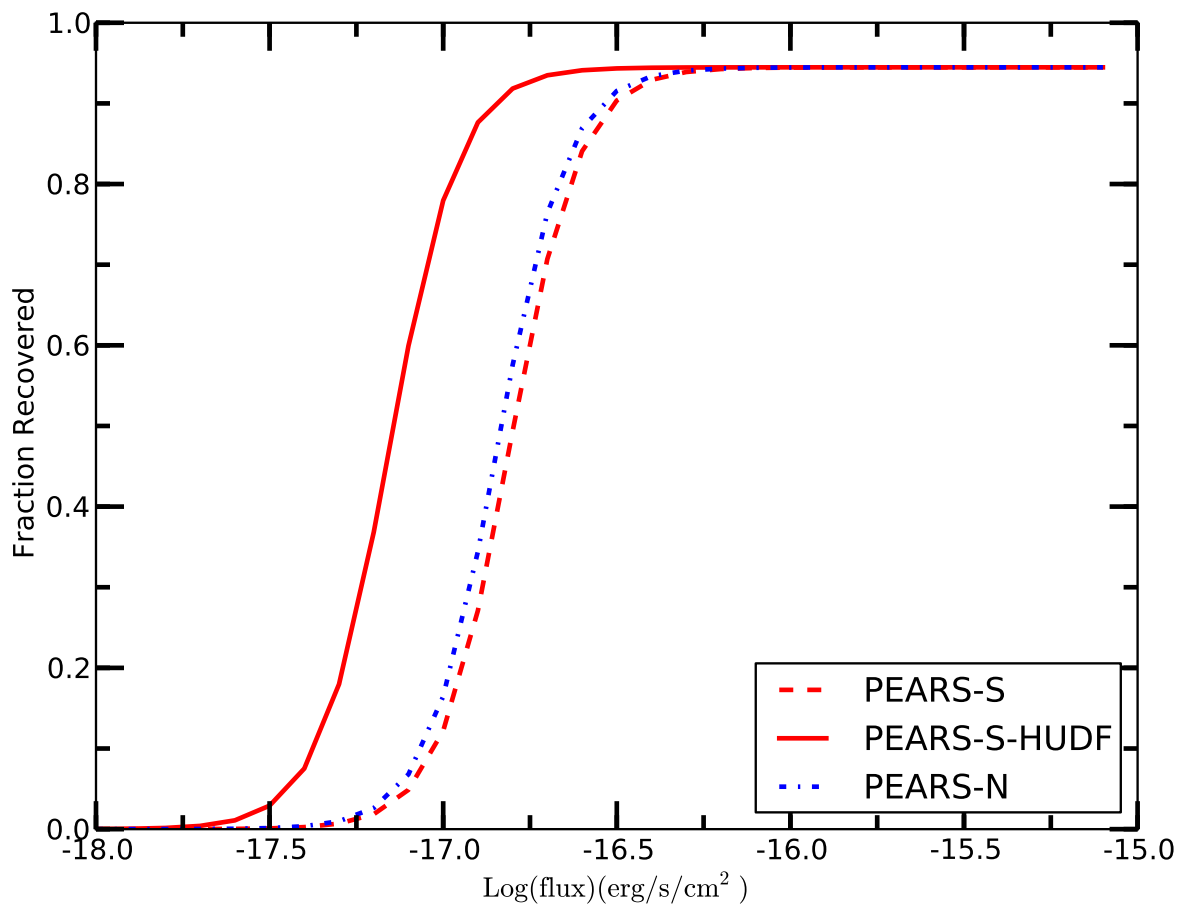


Fig. 5.— PEARS sensitivity to emission-line flux. Based on our simulations, we can reliably ( $> 85\%$ ) detect emission lines with fluxes greater than  $10^{-16.5}$  ( $3 \times 10^{-17} \text{erg/s/cm}^2$ ) over the whole PEARS field while the PEARS-S-HUDF field, which was observed twice as long as each of the other 8 PEARS fields, reaches line fluxes approximately 1.4 times fainter. The 50% line-flux completeness limit is approximately  $10^{-16.7}$  ( $2 \times 10^{-17} \text{erg/s/cm}^2$ ).

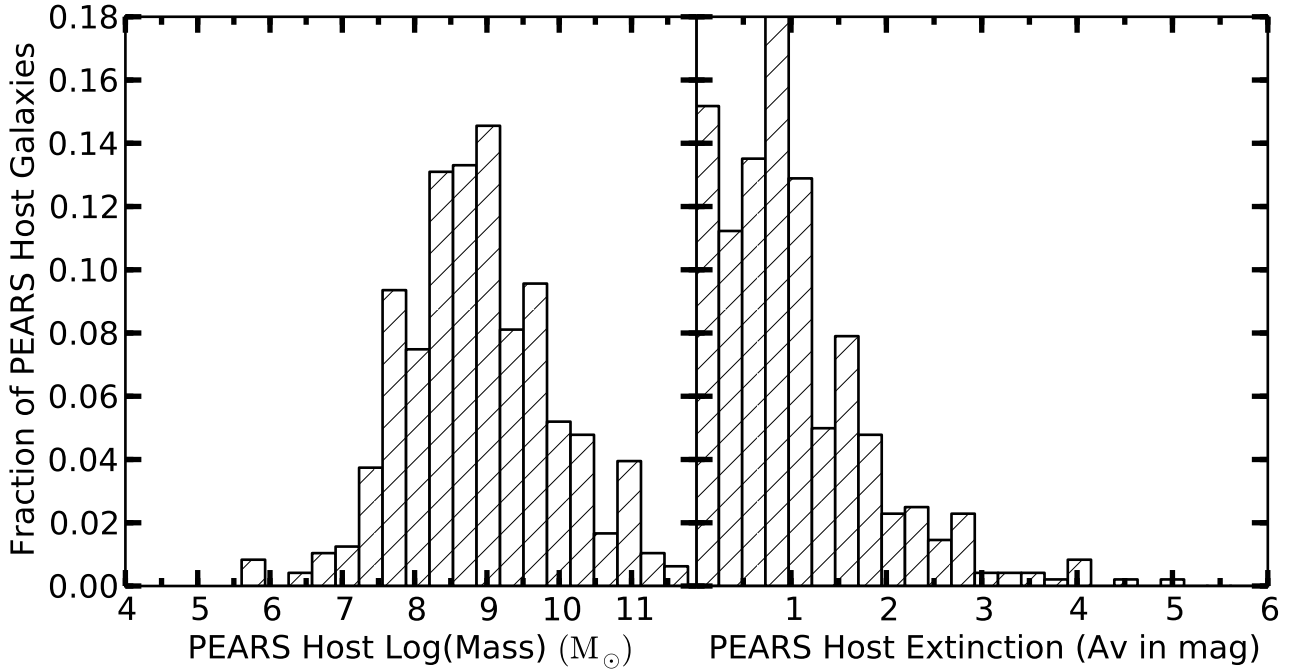


Fig. 6.— Left panel: Histogram of the PEARs emission-line galaxy stellar masses (in  $M_{\odot}$ ) as determined from the SED fitting. We derive a mean stellar mass of  $\text{Log}(\text{mass}) = 8.85 \pm 1.03 M_{\odot}$  ( $1\sigma$ ). Right panel: Histogram of the PEARs emission-line galaxy extinction ( $A_v$  in mag) as determined from SED fitting. A mean extinction of  $A_v = 0.88 \pm 0.93$  mag ( $1\sigma$ ) is derived.



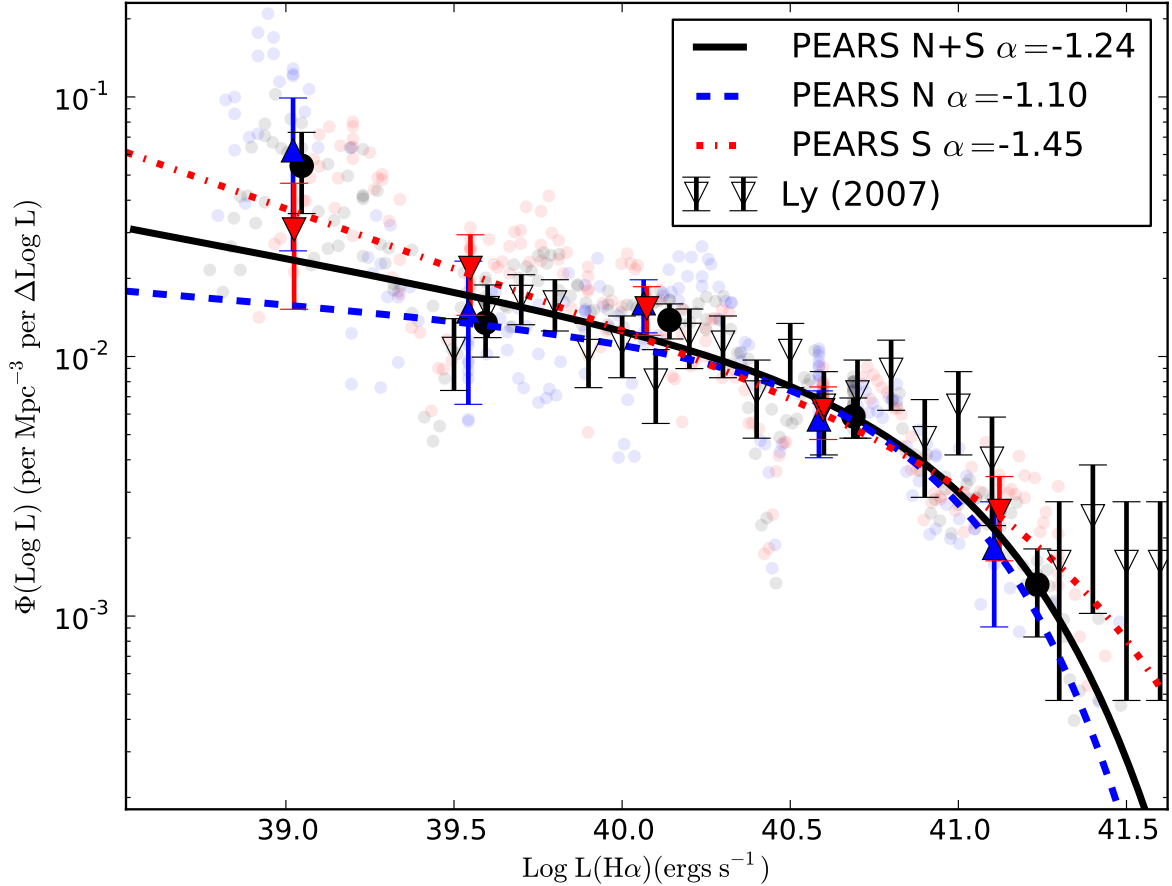


Fig. 7.— PEARS  $H\alpha$  luminosity function at  $0 < z < 0.5$ . We show the  $1/V_{\max}$  results for the full PEARS, PEARS-N and PEARS-S in black circles, blue upright triangles, and red downward triangles, respectively. The fits to the  $1/V_{\max}$  results are shown by the solid black line, blue dashed line, and red dash-dotted line, for PEARS, PEARS-N and PEARS-S, respectively. No significant differences are found between the PEARS-N and PEARS-S fields. We also plot the sample of  $z = 0.4$   $H\alpha$  emitters from Ly et al. (2007), also with no dust correction and excluding objects with  $EW < 50\text{\AA}$  from their sample, to better compare results, and illustrate how PEARS reaches to fainter luminosities for objects that were selected in similar ways.

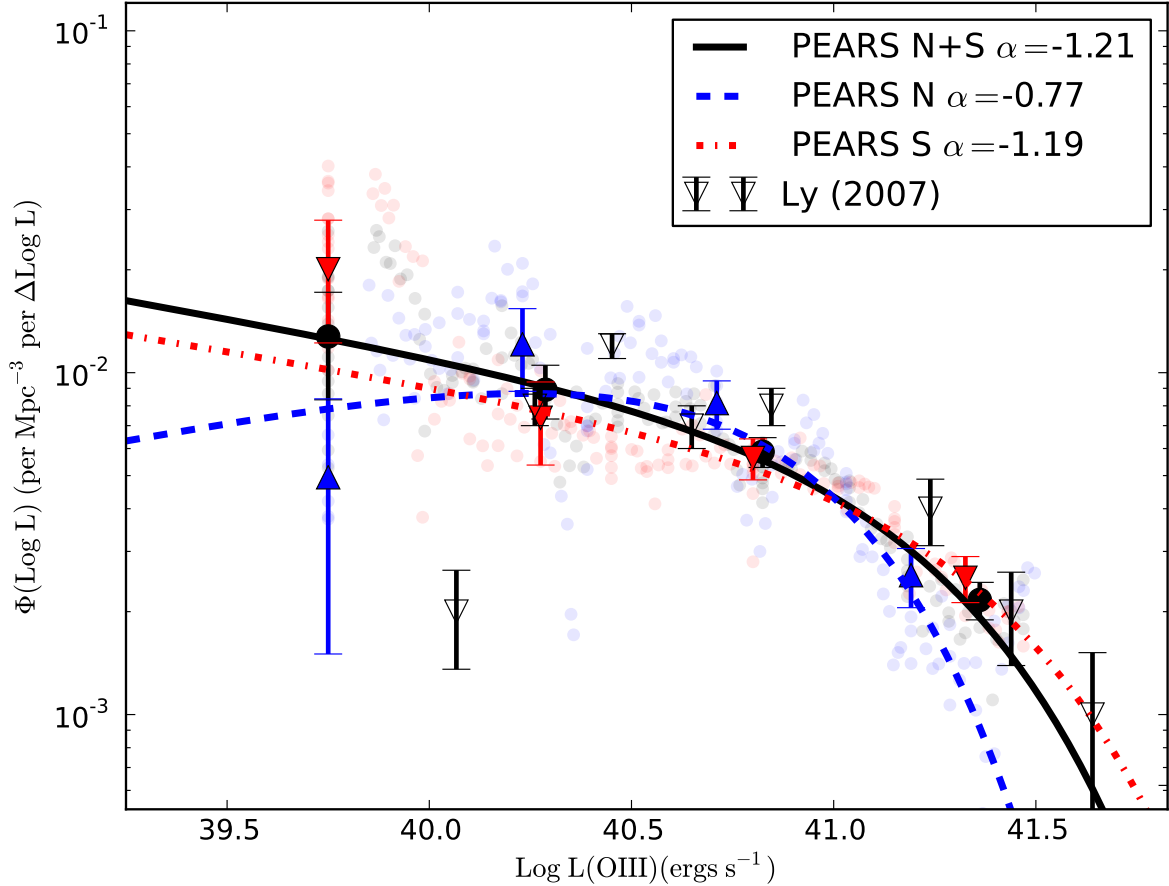


Fig. 8.— PEARS [OIII] luminosity function at  $0.1 < z < 0.9$ . We show the  $1/V_{\max}$  results for the full PEARS, PEARS-N and PEARS-S in black circles, blue upright triangles, and red downward triangles, respectively. The fits to the  $1/V_{\max}$  results are shown by the solid black line, blue dashed line, and red dash-dotted line, for PEARS, PEARS-N and PEARS-S, respectively. No significant differences between the PEARS-N and PEARS-S fields are detected. We also plot the sample of  $z = 0.6$  [OIII] emitters from Ly et al. (2007), also with no dust correction and excluding objects with  $EW < 50\text{\AA}$  from their sample to better compare our results and illustrates how PEARS reaches to fainter luminosities for objects selected in similar ways.

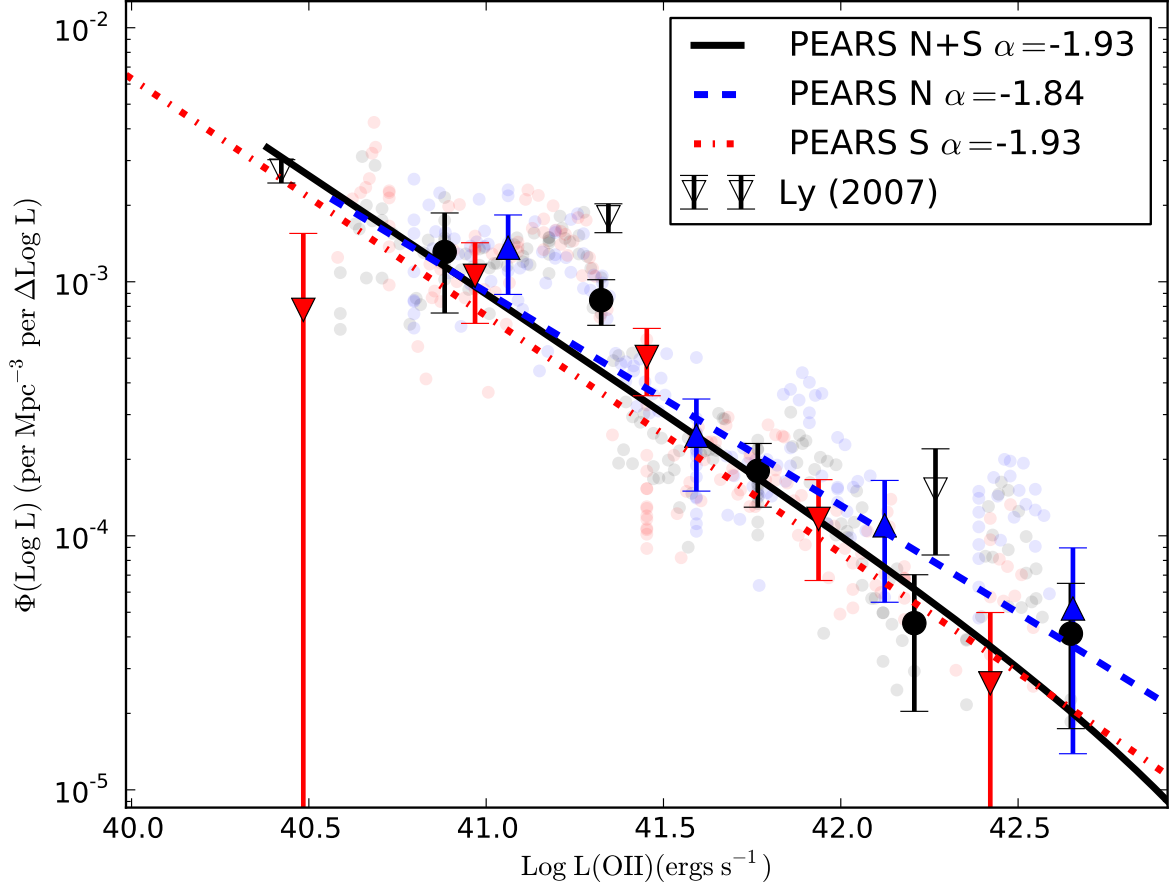


Fig. 9.— PEARS [OII] luminosity function at  $0.9 < z < 1.5$ . We show the  $1/V_{\text{max}}$  results for the full PEARS, PEARS-N and PEARS-S in black circles, blue upright triangles, and red downward triangles, respectively. The fits to the  $1/V_{\text{max}}$  results are shown by the solid black line, blue dashed line, and red dash-dotted line, for PEARS, PEARS-N and PEARS-S, respectively. No significant differences are found between the PEARS-N and PEARS-S fields. We also plot the sample of  $z = 0.9$  [OII] emitters from Ly et al. (2007), also with no dust correction and excluding objects with  $\text{EW} < 50 \text{\AA}$  from their sample, to better compare results.

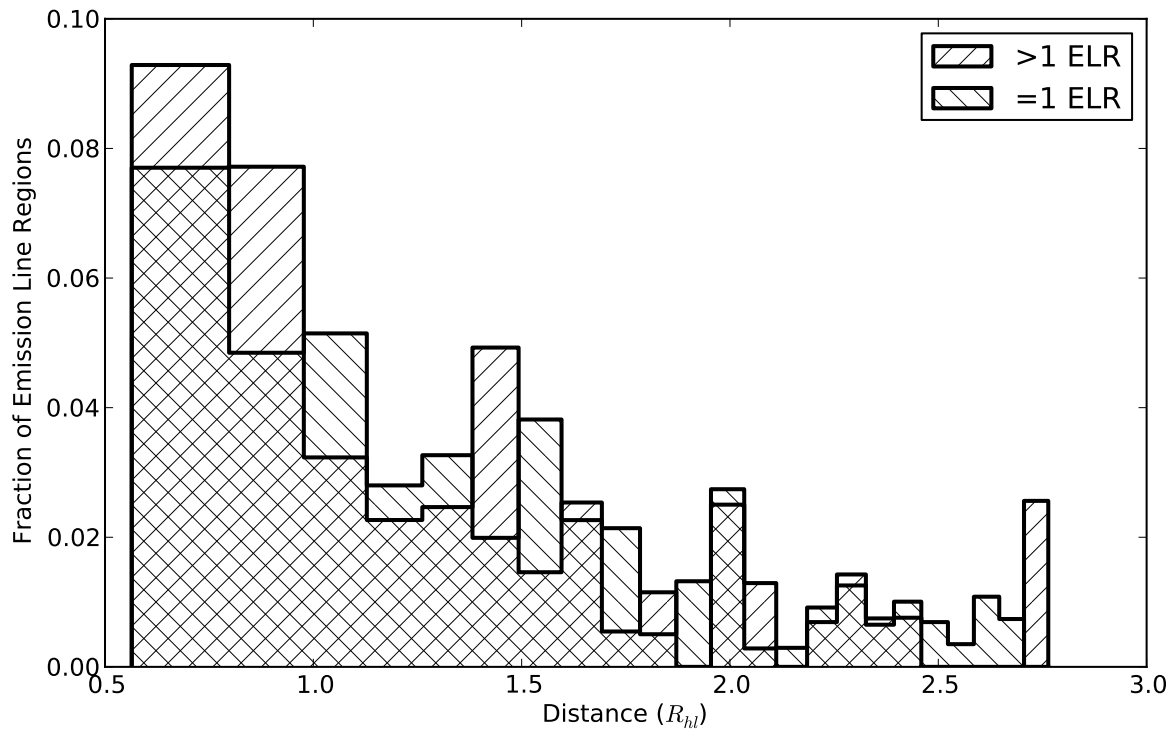


Fig. 10.— Histograms of the distance of the PEARS ELRs from the center of their host galaxies, measured in units of  $R_{hl}$ . Bins sizes were selected to correspond to equal areas. We show the distribution of ELRs in ELGs where only one ELR was identified as well as the distribution of ELRs in ELGs, where more than one ELR was identified. A K-S test p-value of 0.49 indicates that no significant differences exist between the two distributions.

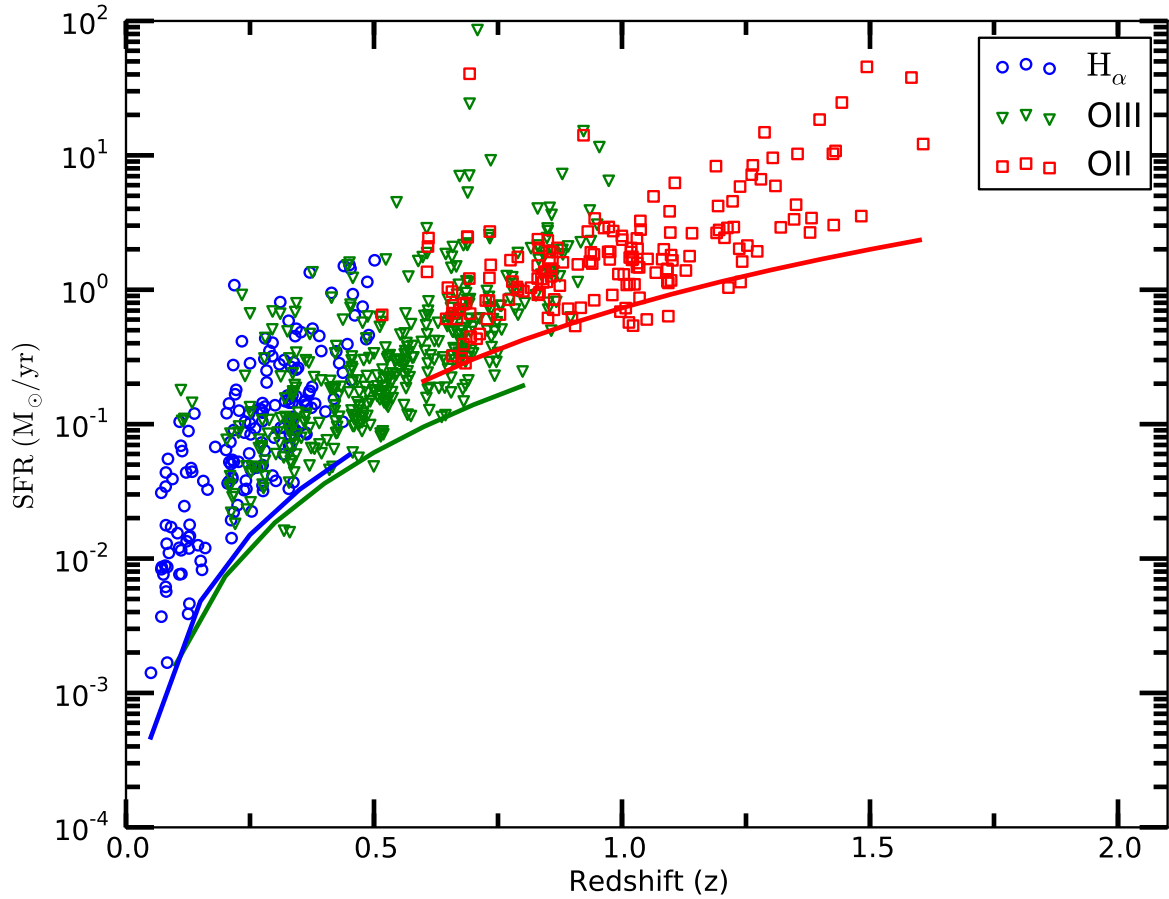


Fig. 11.— The SFR as a function of redshift for the PEARS  $[O\text{III}]$ ,  $[O\text{II}]$ , and  $H_{\alpha}$  ELRs with a line grade greater than 2.5. The solid lines show the SFR corresponding to a flux limit of  $1 \times 10^{-17}$  erg/s/cm<sup>2</sup>, below which most line-emitting sources would not be detected (see Figure 5)

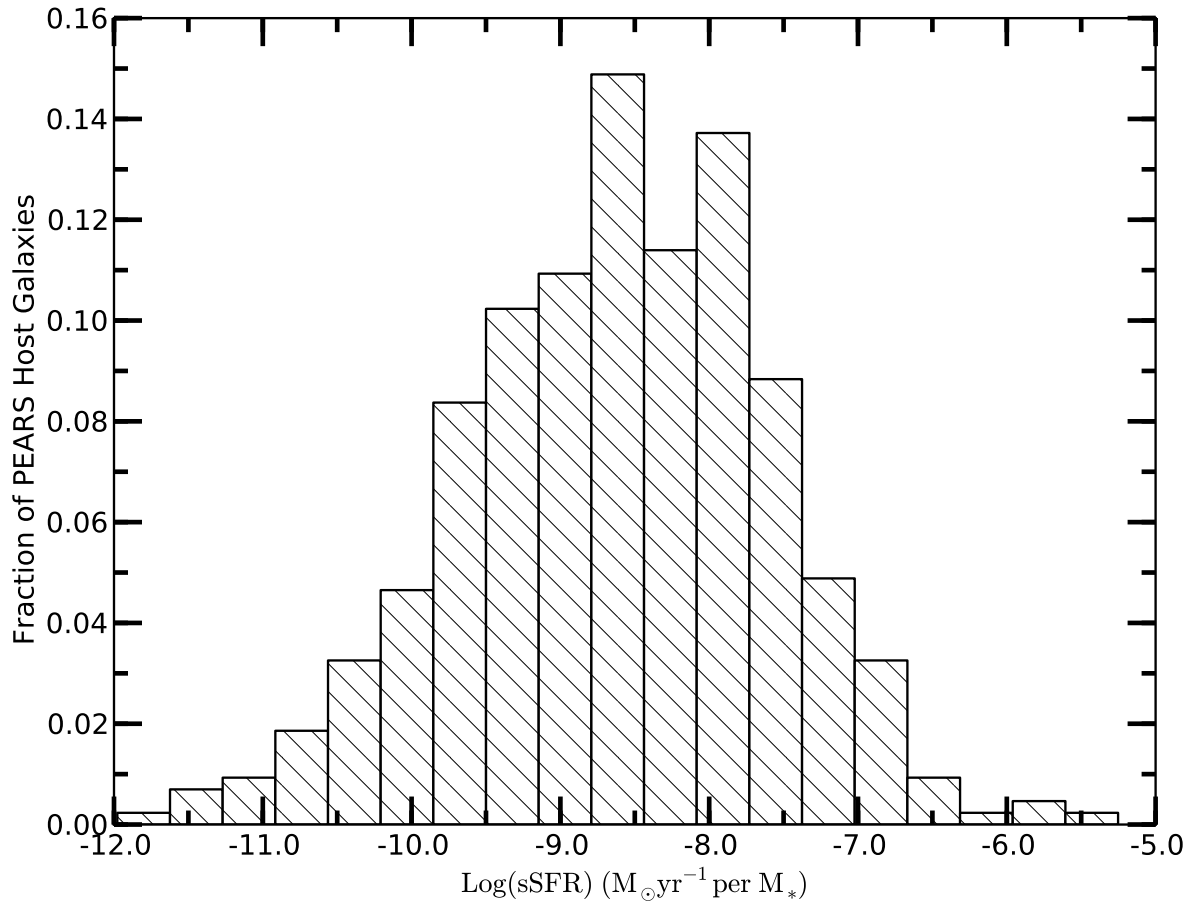


Fig. 12.— Distribution of the specific SFR (sSFR) for the PEARS host galaxies. The sSFR shown were corrected for extinction using the luminosity dependent dust correction from Hopkins et al. (2001).

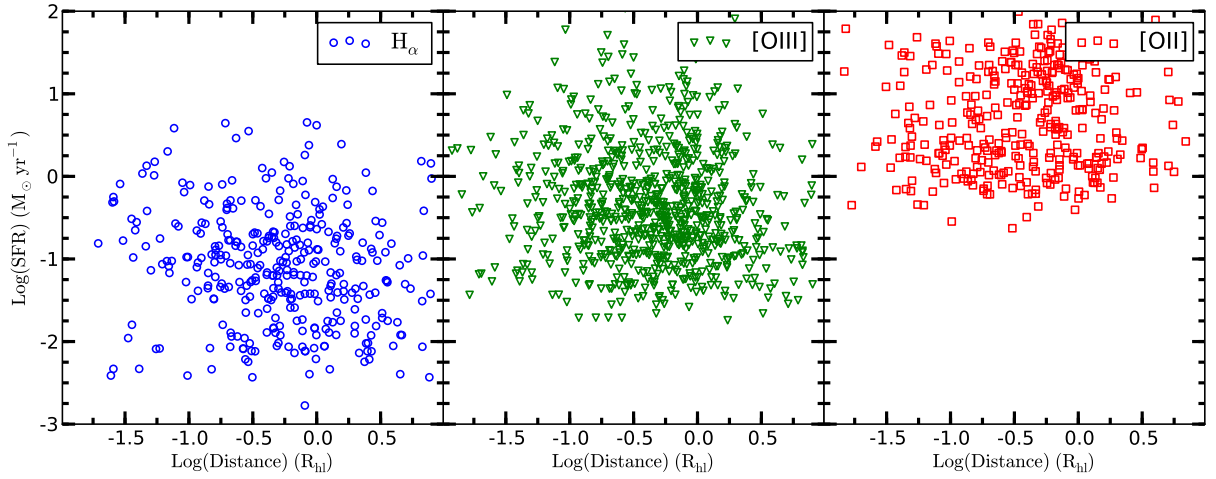


Fig. 13.— The dust corrected SFR of the PEARS emission line regions plotted as a function of their radial position in their host galaxy, normalized to the half light radius of the host galaxy,  $R_{hl}$ ). The amount of star-formation appears uncorrelated with the location of the ELR in the host galaxy with Pearson's correlation coefficients of -0.03, -0.03 and 0.01 for  $H\alpha$ ,  $[OIII]$  and  $[OII]$ , respectively. This indicates no correlation exists between the parameters plotted. These three panels are proxies for the redshift bins of  $0 < z < 0.5$ ,  $0.1 < z < 0.9$ , and  $0.5 < z < 1.5$ , respectively.

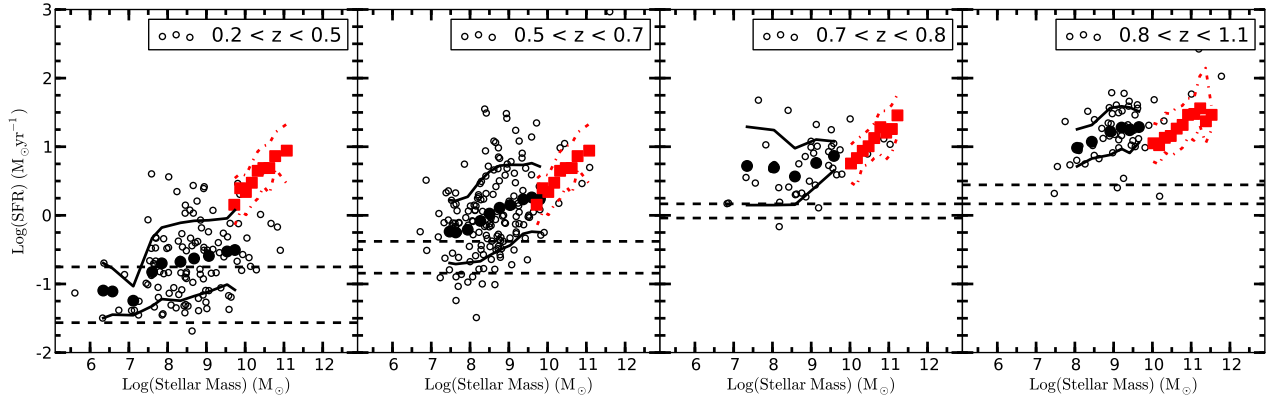


Fig. 14.— Comparison of the dust corrected SFR with Stellar Mass for the ELG sample (open black circles). The data have been binned into 4 redshift ranges for a 1:1 comparison with higher mass star-forming galaxies from the Extended Groth Strip (Noeske et al. 2007). The dash-dotted red line represents the  $\pm 1\sigma$  of the median values of Noeske et al. (2007). The solid black circles represents the median for the ELG sample. The solid black lines represent the  $\pm 1\sigma$  of the median values. The dashed horizontal line represents the 80% completion levels at the minimum and maximum redshifts considered in each panel.



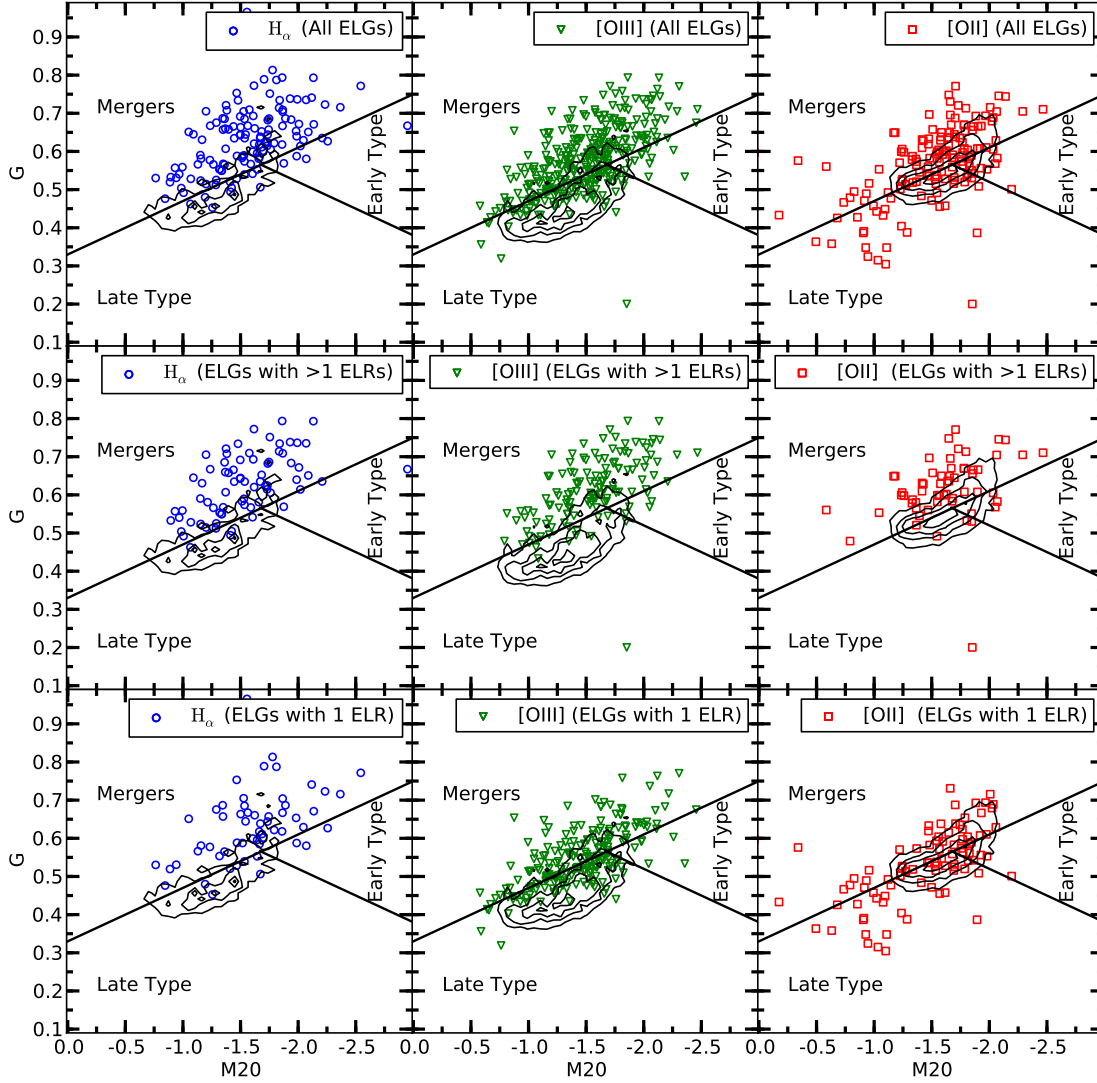


Fig. 15.— Morphology of the PEARS ELGs as parametrized by the Gini and M20 coefficients at the rest-frame wavelength of 4350Å. Top row: PEARS ELGs with [OII], [OIII], and H $\alpha$  ELRs (red squares, green triangles and blue circles, in the left to right columns, respectively). Middle row: PEARS ELGs containing multiple ELRs. Bottom row: PEARS ELGs containing only one ELR. In every panel we show the rest-frame morphology of the GOODS field galaxies (using contours) with photometric redshift estimates ranges of  $0 < z < 0.5$ ,  $0.1 < z < 0.9$ , and  $0.5 < z < 1.5$  (left to right columns), respectively. The galaxy hosts of the emission lines that we detected are nearly all above the line (shown in black) that separates “normal” galaxies (below the line) and “merging” galaxies in the nearby Universe and is taken from Lotz (2004). Most PEARS ELGs are clumpy and have “merger-like”  $G$ - $M_{20}$  values when observed in the rest-frame wavelength of 4350Å.

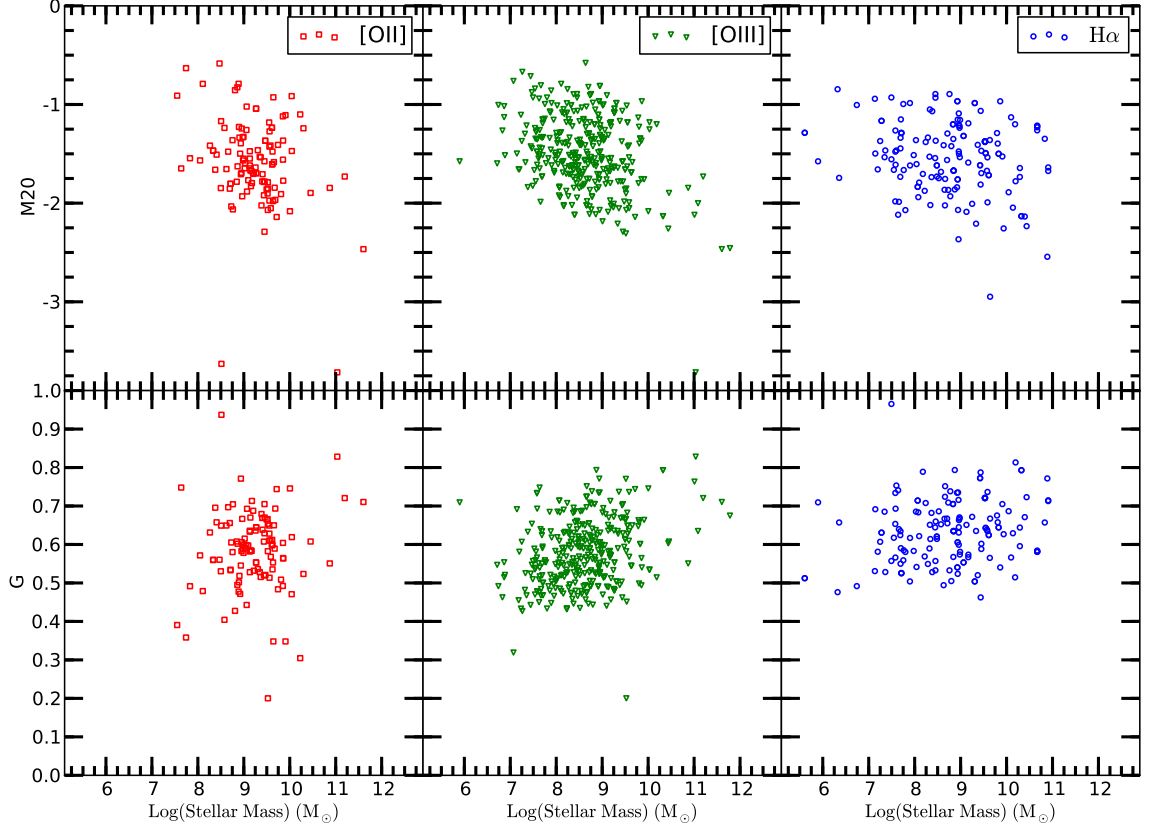


Fig. 16.— Gini coefficient values of the PEARS host galaxies versus their stellar masses, as estimated from SED fitting. The M20 and the Gini values are shown in the top and bottom row, respectively. The [OII], [OIII] and  $H\alpha$  host galaxies are shown separately in the left, middle and right most column respectively. There is little evidence for a strong trend between stellar mass and either the M20 or Gini coefficients in our PEARS emission-line host galaxies, as indicated by Pearson's correlation coefficient values of at most  $\approx 0.16$ . However, a mild decrease in M20, and an increase in the Gini coefficient as stellar mass increases can be seen for the [OIII] and  $H\alpha$  host galaxies (at redshifts of  $0.1 < z < 0.9$  and  $0 < z < 0.5$  respectively).

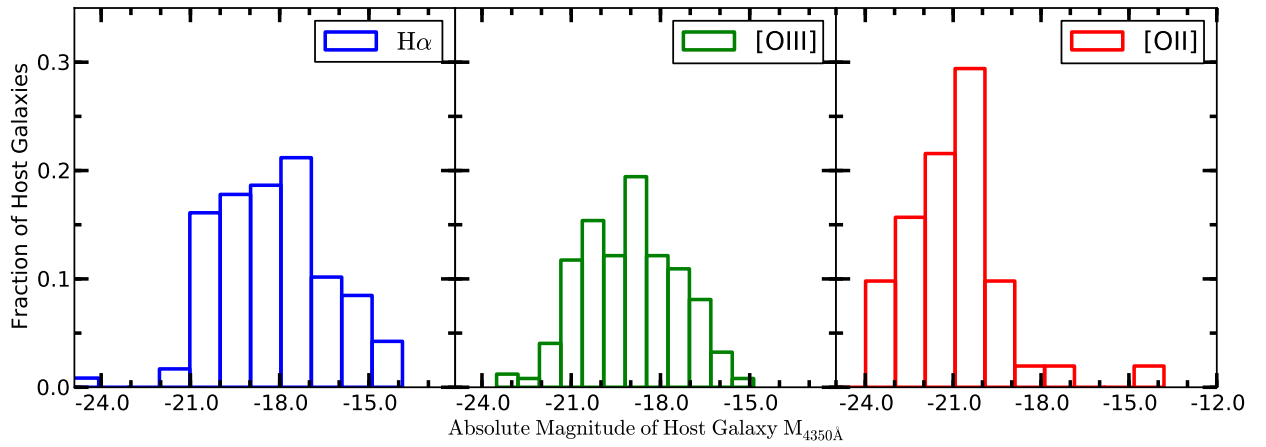


Fig. 17.— Distributions of the 4350 Å rest-frame absolute magnitude of the host galaxies of the PEARS  $H\alpha$ ,  $[OIII]$  and  $[OII]$  emission line (redshift ranges of  $0 < z < 0.5$ ,  $0.1 < z < 0.9$ , and  $0.5 < z < 1.5$ ), respectively.

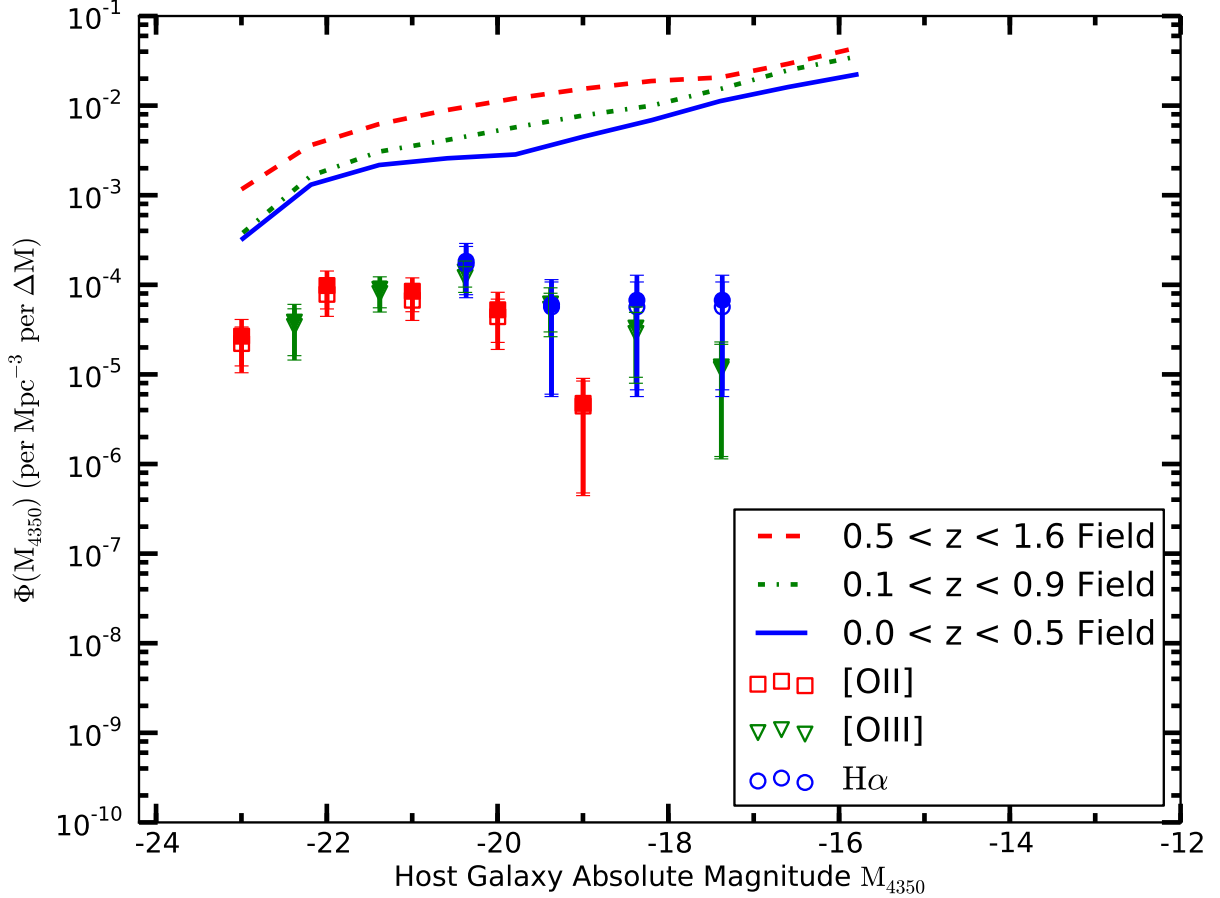


Fig. 18.— Rest-frame 4350Å luminosity functions for the PEARS host galaxies of PEARS H $\alpha$ , [OIII] and [OII] emission lines (symbols with error bars, for the redshift ranges of  $0 < z < 0.5$ ,  $0.1 < z < 0.9$ , and  $0.5 < z < 1.5$ , respectively). Only galaxies with at least one PEARS emission line with with a SFR  $> 6 M_{\odot} yr^{-1}$  are shown (which corresponds to an emission line at  $z = 1.5$  with an observed flux of  $3 \times 10^{-17}$  erg/s/cm $^2$ ). Both the completeness corrected (filled symbols) and uncorrected (open symbols) density estimates are presented. Although the GOODS data are more than deep enough to allow us to detect host galaxies with  $M < -18$  mag at all redshifts (solid curves), we detect no galaxy with  $M > -18$  mag at  $0.5 < z < 1.6$  with [OII] emission.

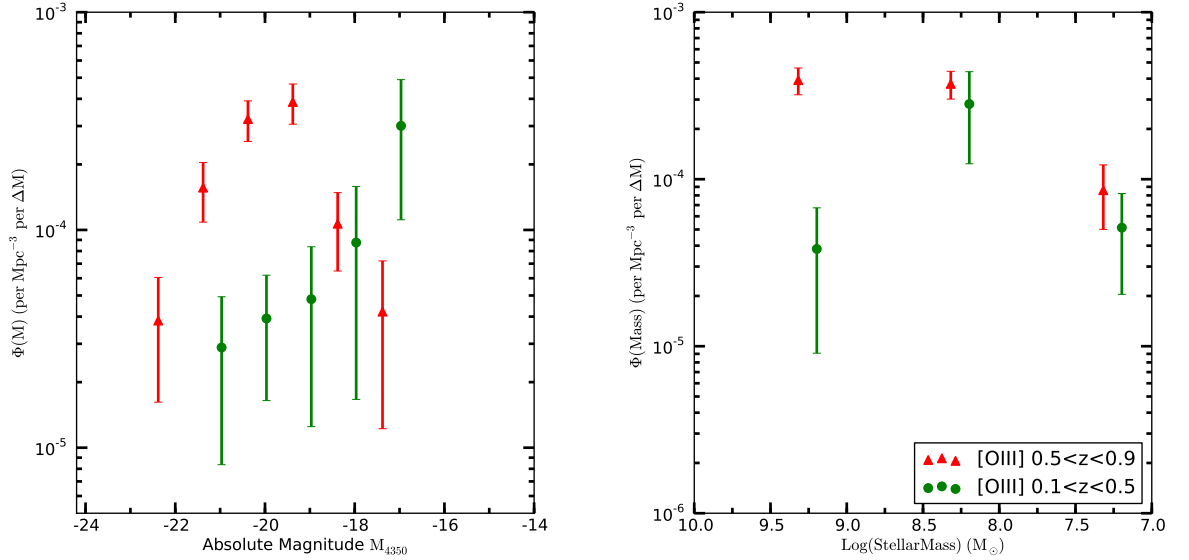


Fig. 19.— Left Panel: Rest-frame 4350Å luminosity function for the host GOODS galaxies, where at least one [OIII] emission-line region was detected with a  $SFR > 1.7 M_{\odot} \text{ yr}^{-1}$  (corresponding to our flux limit at the maximum observable redshift of 0.9). We plot the densities of host galaxies in the lower redshift range of  $0.1 < z < 0.5$  as green circles and the ones at  $0.5 < z < 0.9$  as red triangles. There is a strong decrease in the density of faint ( $M_{4350} > -19$  mag) host galaxies at higher redshifts, that does not exist at lower redshifts. Right Panel: The corresponding host galaxy mass function for the data shown on the left panel. There is a strong, ten-fold decrease in the number density of galaxies with [OIII] emission with stellar masses greater than  $10^9 M_{\odot}$  in the lower redshift bin while the density of [OIII] emitting galaxies remains the same for less massive galaxies.

## REFERENCES

- Alexander, D. M., Bauer, F. E., Brandt, W. N., et al. 2003, *AJ*, 126, 539
- Beswick, R. J., Riley, J. D., Marti-Vidal, I., et al. 2006, *MNRAS*, 369, 1221
- Bertin, E., & Arnouts, S. 1996, *A&AS*, 117, 393
- Bruzual, G., Charlot, S., 2003, *MNRAS*, 344,1000
- Calzetti, D., Armus, L., Bohlin, R. C., et al. 2000, *ApJ*, 533, 682
- Calzetti, D., Kennicutt, R. C., Jr., Bianchi, L., et al. 2005, *ApJ*, 633, 871
- Cardelli, J. A., Clayton, G. C., & Mathis, J. S. 1989, *ApJ*, 345, 245
- Cowie, L. L., Songaila, A., Hu, E. M., & Cohen, J. G. 1996, *AJ*, 112, 839
- Dahlen, T., Mobasher, B., Dickinson, M., et al. 2010, *ApJ*, 724, 425
- Dahlen, T. et al., in prep.
- Drozdovsky, I., Yan, L., Chen, H.-W., et al. 2005, *AJ*, 130, 1324
- Efstathiou, G., Ellis, R. S., Peterson, B. A., 1988, *MNRAS*, 232
- Freedman, D.; Diaconis, P. (1981). "On the histogram as a density estimator: L2 theory".  
*Zeitschrift fr Wahrscheinlichkeitstheorie und verwandte Gebiete* 57 (4): 453476.
- Fujita, S. S., Ajiki, M., Shioya, Y., et al. 2003, *AJ*, 125, 13
- Giavalisco, M., Ferguson, H. C., Koekemoer, A. M., et al. 2004, *ApJ*, 600, L93
- Grogin, N. A et al., in prep.
- Guo, Y., Giavalisco, M., Ferguson, H. C., Cassata, P., & Koekemoer, A. M. 2011, *ApJ*, 735,  
18
- Hinshaw, G., Larson, D., Komatsu, E., et al. 2012, arXiv:1212.5226
- Holwerda, B. W., Pirzkal, N., de Blok, W. J. G., et al. 2011, *MNRAS*, 416, 2437
- Hopkins, A. M., Connolly, A. J., Haarsma, D. B., & Cram, L. E. 2001, *AJ*, 122, 288
- Hopkins, A. M. 2004, *ApJ*, 615, 209
- Juneau, S., Dickinson, M., Alexander, D. M., & Salim, S. 2011, *ApJ*, 736, 104

- Komatsu, E., Smith, K. M., Dunkley, J., et al. 2011, *ApJS*, 192, 18
- Kashikawa, N., Shimasaku, K., Malkan, M. A., et al. 2006, *ApJ*, 648, 7
- Kennicutt, R. C., Jr. 1998, *ARA&A*, 36, 189
- Koekemoer, A. M., Fruchter, A. S., Hook, R. N., & Hack, W. 2002, in *Proc. 2002 HST Calibration Workshop*, ed. S. Arribas, A. Koekemoer, & B. Whitmore (Baltimore: STScI), 33
- Kümmel, M., Walsh, J. R., Pirzkal, N., et al. 2009, *PASP*, 121, 59
- Laidler, V. G., Papovich, C., Grogin, N. A., et al. 2007, *PASP*, 119, 1325
- Lotz, J. M., Primack, J., & Madau, P. 2004, *AJ*, 128, 163
- Lotz, J. M., Jonsson, P., Cox, T. J., & Primack, J. R. 2008, *MNRAS*, 391, 1137
- Lotz, J. M., Jonsson, P., Cox, T. J., & Primack, J. R. 2010, *MNRAS*, 404, 590
- Ly, C., et al. 2007, *ApJ*, 657, 738
- Madau, P., Pozzetti, L., & Dickinson, M. 1998, *ApJ*, 498, 106
- Malkan, M., Teplitz, H., & McLean, I. 1995, *ApJ*, 448, L5
- Maraston C., Daddi, E., Renzini, A., Cimatti, A., Dickinson, M., Papovich, C., Pasquali, A., and Pirzkal, N. 2005, *MNRAS*, 362, 799
- Meurer, G. R. 1995, *Nature*, 375, 742
- Noeske, K. G., Weiner, B. J., Faber, S. M., et al. 2007, *ApJ*, 660, L43
- Noeske, K. G., Faber, S. M., Weiner, B. J., et al. 2007, *ApJ*, 660, L47
- Pirzkal, N., Pasquali, A., & Demleitner, M. 2001, *ST-ECF Newslett.*, 29, 5
- Noeske, K. G., Faber, S. M., Weiner, B. J., et al. 2007, *ApJ*, 660, L43
- Noeske, K. G., Faber, S. M., Weiner, B. J., et al. 2007, *ApJ*, 660, L47
- Papovich, C., & Bell, E. F. 2002, *ApJ*, 579, L1
- Popescu, C. C., Hopp, U., & Elsaesser, H. 1997, *A&A*, 325, 881
- Peng, C. Y., Ho, L. C., Impey, C. D., & Rix, H.-W. 2002, *AJ*, 124, 266

- Pirzkal, N., Xu, C., Malhotra, S., et al. 2004, ApJS, 154, 501
- Pirzkal, N., Xu, C., Ferreras, I., et al. 2006, ApJ, 636, 582
- Pirzkal, N., Burgasser, A. J., Malhotra, S., et al. 2009, ApJ, 695, 1591
- Pirzkal, N., Rothberg, B., Nilsson, K. K., et al. 2012, ApJ, 748, 122
- Ravindranath, S., Giavalisco, M., Ferguson, H. C., et al. 2006, ApJ, 652, 963
- Rhoads, J. E., Malhotra, S., Dey, A., et al. 2001, The New Era of Wide Field Astronomy, 232, 196
- Rothberg, B., & Fischer, J. 2010, ApJ, 712, 318
- Rothberg, B., Fischer, J., Rodrigues, M., & Sanders, D. B. 2013, ApJ767, 72
- Salzer, J. J., Aldering, G. S., Bothun, G. D., Mazzarella, J. M., & Lonsdale, C. J. 1988, AJ, 96, 1511
- Sandage, A., Tammann, G. A., & Yahil, A. 1979, ApJ, 232, 352
- Schechter, P. 1976, ApJ, 203, 297
- Straughn, A. N., Meurer, G. R., Pirzkal, N., et al. 2008, AJ, 135, 1624
- Straughn, A. N., Pirzkal, N., Meurer, G. R., et al. 2009, AJ, 138, 1022
- Takahashi, M. I., Shioya, Y., Taniguchi, Y., et al. 2007, ApJS, 172, 456
- Taylor-Mager, V. A., Conselice, C. J., Windhorst, R. A. & Jansen, R. A. 2007, ApJ, 659,162